UNIVERSITÀ DEGLI STUDI DI PADOVA

Dipartimento di Fisica e Astronomia "Galileo Galilei"

Master Degree in Physics

Final Dissertation

Commissioning of the AGATA gamma-ray tracking array

Thesis supervisors

Dr. José Javier Valiente Dobón

Dr.ssa Rosa María Pérez Vidal

Candidate

Filippo Angelini

Academic Year 2021/2022

The Advanced GAmma Tracking Array (AGATA) is a European project for a 4π new-generation γ-ray tracking spectrometer. Thanks to the digital electronics, the traces of the single interactions of the photons are acquired to perform Pulse Shape Analysis (PSA) and localize the interaction points in the HPGe crystals with a precision up to 5 mm. Subsequently, the application of γ-ray tracking algorithms can reconstruct the trajectories of the γ rays within the detector.
AGATA has performed a rich science program using both radioactive and stable ion beams in several European laboratories, coupled to different complementary detectors. In the second half of 2021, AGATA was installed at the Legnaro National Laboratories (LNL) and its experimental campaign started at the end of May 2022. Before the actual experimental campaign started, a series of commissioning experiments were planned to test both the AGATA array and the available complementary detectors. Such first tests are essential to verify the functioning of all the parts of the setup and evaluate the capabilities of the array in the new configuration with the most recent upgrades.
The work in this master thesis focuses on the description and optimization of the processing of the AGATA data and the assessment of the detector performances both with γ-ray sources and during the first in-beam commissioning experiment.
All the preparatory stages for the operation of AGATA are introduced, from the electronics and the support systems for the detectors, to the sorting of the raw data. The data processing envisages different stages, starting by the local level processing that handles the crystals separately. Energy calibrations, time calibrations and cross-talk corrections are applied to ensure a good performance of the PSA. The PSA algorithm provides the position, energy and time of each interaction point of the γ rays with accuracy for the tracking algorithm. Additionally, the PSA provides the information for the neutron damage correction for an improved energy resolution. Finally, a global level processing merges the information from the individual crystals and tracking is performed, combining multiple interactions to reconstruct a larger fraction of full-energy peak events.
In this work, all the steps of the AGATA processing were examined and optimized up to the tracking reconstruction. The optimization was done by tuning a set of parameters that are obtained through measurements with radioactive sources. The output γ-ray spectra of the sources were analyzed to assess the performances of AGATA in terms of energy resolution, efficiency and peak-to-total ratio. Simulations were also performed for the same radioactive sources and efficiency curves were compared for the measured and simulated data.
In the thesis, the in-beam performances of the AGATA array in the first commissioning experiment were studied, where the detector was coupled to the PRISMA magnetic spectrometer. The studied reaction consisted of a multi-nucleon transfer with a ^{32}S beam at 160 MeV on a ^{124}Sn target. The different transfer channels were selected thanks to the A and Z identification in PRISMA and the γ rays associated to the populated energy levels were observed in coincidence with AGATA after the Doppler correction of the photons emitted in flight. The Doppler-corrected spectra for the products of the $-2p$ transfer channel, corresponding to the nuclei ^{30}Si and ^{126}Te, were analyzed and level schemes were constructed with the observed γ rays.

Contents

Chapter 1

Introduction

1.1 Germanium detectors for γ-ray spectroscopy

The objective of the research in nuclear physics is to investigate the nucleon-nucleon interaction in the nuclear medium. Certain phenomenologies of the nuclear interaction require extreme conditions to be studied, therefore the observation of exotic nuclei, which lie far from the valley of stability, has become an important testing field for nuclear structure studies. Thanks to the use of new-generation Radioactive Ion Beams (RIB) facilities, a larger variety of exotic nuclei are accessible. In Europe, such technologies are available at HIE-ISOLDE (CERN, Geneva, Switzerland) and will be available at FAIR (Darmstadt, Germany), SPIRAL2 (Caen, France) and SPES (Legnaro, Italy).

In the past decades, high-resolution γ-ray spectroscopy has become a key tool for nuclear structure studies. This is because γ rays are emitted in the de-excitation of nuclear levels, and the related observables contain relevant information about the single-particle and collective features of the states.

In particular, the use of germanium detectors has brought significant improvement to the field of γ-ray spectroscopy. The major advantage of these detectors is having a high energy resolution that allows to see transitions which are very close in energy, which a detector such as a NaI scintillator would not resolve. The good energy resolution of the germanium is due to the small band gap in the structure of the semiconductor, which is about 0.7 eV. This leads to a large production of electron-hole pairs and a high resolution capability from the high number of charge carriers. However, a small band gap brings the thermal excitation of the electrons at room temperature to cause significant leakage current. To avoid this effect, the germanium crystals must be cooled down to a temperature of 77-90 K using liquid nitrogen. In order to obtain a larger depletion region in the semiconductor when a biasing voltage is applied, the impurity concentration in the germanium should be minimized. This is why the current technology for γ-ray spectroscopy uses High-Purity Germanium (HPGe), where the impurity level is very low [1]. Since the 1980s, a new configuration was designed for germanium detectors in order to obtain a

higher peak-to-total ratio: the crystals where surrounded by anti-Compton shields. These were bismuth germanate (BGO) scintillator crystals that acted as veto for the events with a γ ray escaping the germanium due to Compton scattering, because in this case, the energy collected in the germanium is not the full energy information of the photon and it would contribute to the background. With this technique, the peak-to-total ratio in the γ-ray spectra is increased significantly, but the BGOs cover a large part of the angular range, decreasing the total efficiency of the detector. During the 1980s and 1990s, 4π Compton-suppressed HPGe arrays represented the frontier of the spectroscopy advancement [2], with spectrometers such as EUROBALL [3] and GAMMASPHERE [4]. These arrays allowed for a significant improvement of the sensitivity, but implied a limitation in the geometrical efficiency of the germanium crystals for the solid angle occupied by the Compton-shield detectors.

The most recent developments in γ-ray spectroscopy come from position sensitive HPGe detectors and the use of tracking algorithms. In the γ-ray tracking arrays, in fact, thanks to the electrical segmentation of the germanium crystals and the high-rate digital acquisition system, it is possible to use pulse shape analysis methods to obtain precise energy, time and position information for each interaction of the photons in the crystals. The accuracy on the interaction position, and therefore on the γ-ray emission direction, is important to correct the Doppler energy shift that affects γ rays emitted in flight by ions at relativistic velocities. Especially, this high level of sensitivity is needed for spectroscopy with high-intensity radioactive and stable beams and previous generation γ-ray detectors were not able to reach it. From the interaction positions in the germanium crystals, tracking algorithms can be used to reconstruct the full trajectory of the Compton-scattered photons, recovering the information of the original emitted γ ray. By summing up partial energy losses in the Compton interactions, a higher fraction of full-energy events can be reconstructed and this improves the peak-to-total ratio in the γ-ray spectra. Simultaneously, removing the anti-Compton shields, a broader solid angle can be covered by the active volume of the detector obtaining a larger efficiency of the array.

The tracking array technology represents a significant advance in γ-ray detection which can have applications in medical imaging, astrophysics, nuclear safeguards and radioactive waste monitoring, along with a higher level of sensitivity for studies in nuclear structure [5]. Currently, two arrays of this generation are operational globally: the Advanced GAmma-ray Tracking Array (AGATA) [5] is the European state-of-the-art array for γ-ray spectroscopy, while the GRETA [6] project was developed in the United States.

1.2 AGATA

AGATA [5] is a European collaboration for the development of a full 4π γ-ray tracking array. The array is designed to be moved across Europe, working at the major nuclear physics laboratories in order to be used with a variety of beams and complementary detectors. Until now, the whole array has travelled four times and new germanium crystals were added at each new step. The first experimental campaign was at INFN-LNL (Legnaro, Italy) with 15 crystals [7], then at GSI

(Darmstadt, Germany) with up to 21 crystals [8], later at GANIL (Caen, France) with 45 crystals in the setup [9]. AGATA has moved back to the INFN-LNL, where the installation started in April 2021 and the complete set-up of the support systems and the acquisition chain was finalized in April 2022. The objective is to reach a 2π angular coverage during the experimental campaign at LNL [10].

The AGATA data processing involves different successive steps, starting from the local level processing where every crystal is treated individually. In this stage, calibrations and corrections are applied to perform the Pulse Shape Analysis (PSA) algorithm in the optimal conditions. Thanks to the PSA, each interaction in the crystal is characterized by precise position, energy and time information. After the PSA, corrections for neutron damage are applied to the detectors and the spectra are recalibrated. The global level processing starts with the merging of the information from all crystals and from other ancillary detectors and successively, the tracking algorithm is performed to increase the efficiency and peak-to-total ratio of the peaks in the γ-ray spectra.

All these steps of the processing need to be optimized by tuning parameters that are obtained through the measurements with multiple γ-ray sources. In this work, the steps of the optimization will be described in detail and the performances of the array will be evaluated with measurement with radioactive sources, in terms of resolution, efficiency and peak-to-total.

1.3 Commissioning experiments at INFN-LNL

In order to exploit at best the performances in γ-ray observation of AGATA, it is very important to combine it to complementary devices that give a higher selectivity on the reaction channel. In the current installation at LNL, AGATA is coupled to the PRISMA magnetic spectrometer [11] and additional complementary instruments can be placed inside the reaction chamber, such as the SPIDER silicon detector [12] or the PLUNGER device [13].

In order to assess the performance of the AGATA array in the new configuration, as well as to check the functioning and to show the capabilities of the coupling to the available complementary devices, a series of commissioning experiments were scheduled before the start of the actual experimental campaign.

The current work focuses on the first of these commissioning experiments, where the setup involved the PRISMA spectrometer coupled to AGATA. The studied reaction is a multi-nucleon transfer process involving a ^{32}S beam at 160 MeV (5 MeV/u) impinging on a ^{124}Sn target. For the target, two thicknesses were used: 0.5 mg/cm^2 and 2.5 mg/cm^2. The calculated cross sections for the transfer channels are shown in fig. 1.1 and suggest that the most probable channels, other than the elastic one, are the $-1p$, $+1n$ and $+2n$. The entrance of PRISMA was placed at 55° with respect to the beam direction, close to the grazing angle. Eight days of beam time were used for the commissioning measurements of the AGATA+PRISMA setup.

At the start of the experiment, a measurement was performed with the ^{58}Ni+^{197}Au with an

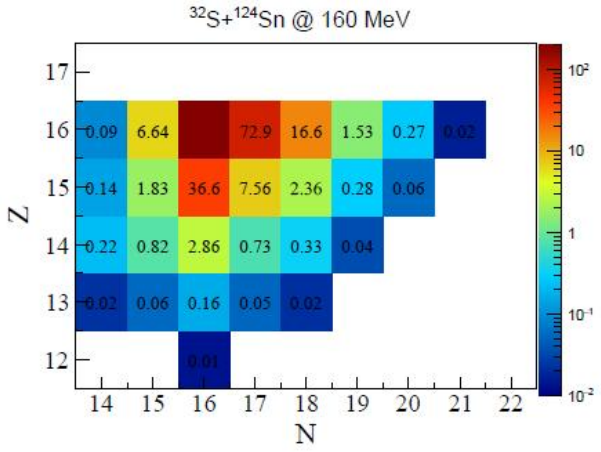

Figure 1.1: Total transfer cross sections in mb predicted with GRAZING for the ^{32}S+^{124}Sn reaction at 160 MeV. Taken from [14]

energy of 250 MeV for the ^{58}Ni beam, which is $\sim 20\%$ below the Coulomb barrier, in order to have Rutherford scattering as dominant reaction process. This reaction was used as a test to set the proper electronic thresholds in the PRISMA electronics and check the performance of the spectrometer at different rates.

The AGATA-PRISMA coupling has the purpose of testing and evaluating the in-beam performances of both devices, as well as the coincidence between the two. As for AGATA, the test concerns the stability of the DAQ, the Pulse Shape Analysis and the Tracking algorithm. The electronics for PRISMA was also recently upgraded and an in-beam test is necessary to verify its functioning [14]. The ultimate goal is to verify the quality of the γ-ray spectra in coincidence with a selected ejectile isotope, thanks to the A and Z identification from PRISMA. An essential part of the analysis is the Doppler correction of the spectra thanks to the information from the AGATA PSA, the γ-ray tracking and PRISMA.

1.3.1 Overview of the work

In the next chapter (chap. 2), a technical description of the detectors and main features of AGATA and PRISMA will be presented. The following chapter (chap. 3) will focus on the data processing in the AGATA+PRISMA setup, with a detailed description of all the steps in the AGATA data sorting from the raw signals to the tracked γ-ray spectra. Next, the results of the testing and optimization of AGATA with radioactive sources will be shown (chap. 4) and its performances will be presented, in terms of energy resolution, efficiency and peak-to-total ratio. Chap. 5 will include the description of the analysis of the commissioning experiment and a focus on one reaction channel: the $-2p$ transfer that populates ^{30}Si and ^{126}Te, where the γ-ray Doppler-corrected spectra will be analyzed and level schemes will be built with the observed transitions. In the final chapter (chap. 6), the work will be summarized and conclusions will be drawn from the results of the analysis.

Chapter 2

Experimental Setup

2.1 The accelerator complex at the INFN-LNL

The commmissioning experiment was performed at the Legnaro National Laboratories (LNL) in Legnaro (Padova, Italy) [15]. The LNL are one of the major research centres for nuclear physics in Italy. In this facility, stable beams are delivered to different experimental halls for experiments on nuclear physics, nuclear-astrophysics and inter-disciplinary physics. The main complex for the acceleration of heavy ions is made of the 14.5 MeV Van de Graaf TANDEM-XTU accelerator [16], the ALPI linear accelerator based on superconducting radio-frequency cavities and the positive ions injector PIAVE [17].

The Tandem accelerator is a two-stage electrostatic accelerator made of a horizontal tank with the high-voltage terminal at its center. It can accelerate ions from protons to ^{197}Au produced by a negative sputtering source. The negative ions are accelerated by the first half of Tandem and they cross a stripper foil placed at the center of the tank, where electrons are removed from the ions, leaving them at a positive charge state. The positive ions are then accelerated by an opposite voltage difference in the second half of the tank. The Tandem accelerator can be used in standalone mode or as an injector for the ALPI superconducting linear accelerator, when higher energies are required for the beam.

The ALPI post-accelerator system is made of a series of quarter-wave resonator cavities (QWR) operated at liquid He temperatures. It can accelerate ions provided by either Tandem or by the PIAVE injector, which is an instrument that acts as a first accelerator stage after the production of positive ions with an ECR source at high intensity [17].

Along the beam line, optical elements such as magnetic quadrupoles and dipoles are used respectively to focus the beam and steer it to the experimental hall.

The beam is delivered to the AGATA reaction chamber, where different targets are mounted on a ladder holder that can be rotated and shifted from the outside. On the target holder, a quartz collimator is used to help center and focus the beam in a narrow spot thanks to a monitoring

camera mounted on a small window in the chamber.

2.2 AGATA

The Advanced GAmma Tracking Array (AGATA) is a European tool for high-precision γ spectroscopy [5]. Its capabilities rely on the high energy resolution of high-purity germanium (HPGe), combined with the possibility to perform a Pulse Shape Analysis (PSA) algorithm and consequently a tracking algorithm. The PSA is used to locate the interaction points of the γ rays in the germanium and can be performed thanks to the segmentation of the AGATA crystals and the fast digital acquisition electronics. The tracking algorithm uses the information of position, time and energy of each interaction obtained by the PSA to reconstruct the trajectory of the Compton-scattered γ rays within the crystals and recover a higher photo-peak efficiency and peak-to-total ratio.

2.2.1 AGATA detectors

The AGATA array is composed of modular detectors called AGATA Triple Clusters (ATCs), made by 3 HPGe crystals inside a tapered capsule. The three crystals in one ATC are manifactured in slightly different ways, and in each cluster, crystals A, B and C can be distinguished. Each Ge crystal has a diameter of 8 cm and a length of 9 cm, and is electronically segmented 6-fold in both the longitudinal and radial directions, with a total of 36 segments (see fig. 2.1). The longitudinal segmentation is labeled by a number from 1 to 6, where a lower number corresponds to a segment closer to the center of AGATA, and the radial segmentation is indicated by a letter from A to F. A single segment is then labeled with the letter from the radial sector and the number from the longitudinal section, *e.g.* segment A1. The total number of output channels for one crystal is 38: 36 from the segments on the outside of the crystal and 2 from the common core contact at the center (one with low gain, one with high gain). The collection of the signal from the electrons happens at the core contact and the holes are collected at the contacts of the segments. This means that the signal amplitude measured by the common core contact equals the sum of the signals in the segments for each interaction.

To achieve the best performance, the germanium needs to be cooled down to 80 K, which is reached by placing the triple cluster in a cryostat with a system for the periodic filling with liquid nitrogen. The triple clusters are mounted on a honeycomb structure with a 0.5 mm space between the sides of two neighbouring ones, with the smallest sides facing the center of the reaction chamber, in order to achieve a uniform coverage of the solid angle.

Each cluster is provided with a Detector-Support System (DSS), which consists of the low- and high-voltage power supplies, the LN_2 filling system and an uninterruptable power supply. The monitoring and the setting of the parameters for these services are performed remotely with a software. The operational bias voltage of the crystals is ~ 5 kV.

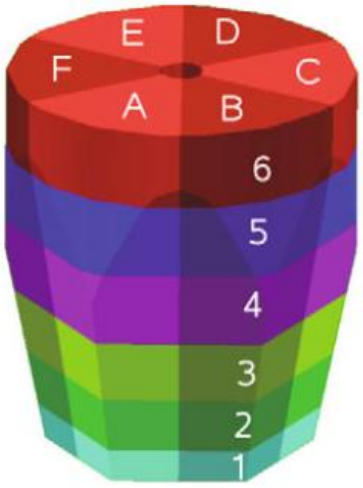

Figure 2.1: Segmentation of the AGATA HPGe crystal

2.2.2 Readout electronics

The output signals of each crystal are fed into a preamplifier module. In order to have fast and clean signals to perform Pulse Shape Analysis (PSA), the charge-sensitive preamplifiers [18] are mounted directly on the ATCs and have both a warm and a cold part. Their differential output is brought through MDR cables to the digitizer modules. The new generation digitizers have a 100 MHz sampling rate and a 14-bit resolution, and they consist of three modules each, therefore one box serves one ATC for all three crystals. The digitizers are also subject to overheating, therefore they have their own water cooling system. There are seven MDR output cables for each crystal, which carry the signals for the six segments, plus the core with two different gains. Thanks to Field Programmable Gate Arrays (FPGAs), the digitized signal is pre-processed with a trapezoidal filter to extract the trigger and energy signal. For each crystal, the core signal is taken as trigger. With every local trigger, a request is sent to the Global Trigger and Synchronization system (GTS) which can be coupled to a Trigger Processor (TP) to select events under the needed experimental conditions, *e.g.* when the γ events must be in coincidence with an event detected by PRISMA. The output of the digitizers is converted to an optical signal and brought through fibers to the Global Gigabit Processor (GGP) boards on the acquisition machines, which are able to sustain an incoming data rate of 2 Gbps per channel.

2.2.3 Configuration at LNL during the commissioning experiment

For the first commissioning experiment, 9 ATCs were mounted on the honeycomb structure. With respect to the last configuration in GANIL, many of the detectors were changed or repaired, also due to the significant neutron damage that some crystals suffered from, at the end of the previous experimental campaign. The look-up table of the mounted detectors using the AGATA collaboration nomenclature for crystals and ATCs is shown in table 2.1. The position number

Table 2.1: Look-up table of the AGATA crystals in the configuration of the first commissioning. The numbering is referred to the convention of the AGATA collaboration.

Position	ATC	Crystal		
		A	B	C
0	12	6	5	1
1	10	11	6	12
2	17	16	17	13
6	6	8	9	2
7	14	14	10	16
8	3	2	7	7
9	18	17	18	18
10	15	13	15	11
11	1	10	11	9

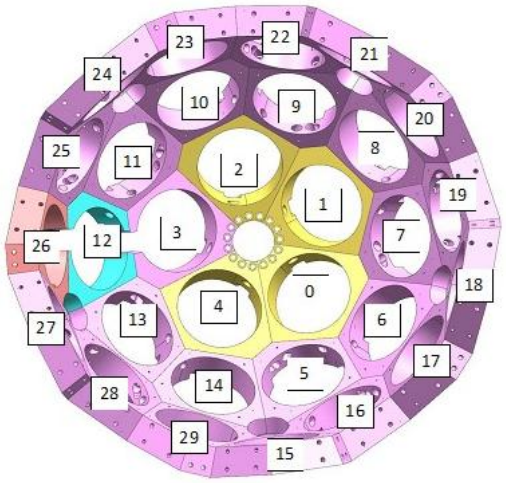

Figure 2.2: Scheme of the AGATA honeycomb with the position numbers for the ATCs.

refers to the numbering on the honeycomb that is shown in fig. 2.2. A picture of all mounted clusters during the first commissioning is shown in fig. 2.3, where the crystals A, B, C are labeled for each ATC.

The mechanical structure that holds AGATA is mounted on the same rotating platform that holds PRISMA and the center of the honeycomb is oriented at 180° from the entrance of the PRISMA spectrometer. This means that, depending on the reaction, both the spectrometer and AGATA rotate with respect to the incoming beam line. This is why in the scheme in fig. 2.2, positions 3, 12 and 26 cannot be used for placing ATCs, since the beam line has to pass from one of these, depending on the angle of PRISMA.

The reaction chamber (shown in fig. 2.4) is connected to the entrance of PRISMA and the side that is facing AGATA has a spherical shape of 170 mm of outer radius, made of a 2 mm aluminum layer [19]. The two common modes of operation of AGATA are in the nominal position, where the center of the reaction chamber (the target) is concentric with the center of the honeycomb and the ATCs, which corresponds to a distance of 235 mm of the faces of the ATCs from the target, and at compact position, where AGATA is shifted closer to the reaction chamber to increase the efficiency, and the distance between the ATCs and the target is approximately 180 mm [19]. The whole first commissioning experiment was performed at nominal position.

2.2.4 Pulse Shape Analysis

The tracking algorithm for the reconstruction of the γ-ray trajectories inside the array requires the position, time and energy of each interaction point of the incoming γ rays. Using the Pulse Shape Analysis (PSA) algorithm [5] it is possible to obtain this information before the tracking reconstruction. The PSA compares the measured signals traces in each segment of one crystal with a library of segment-by-segment traces that correspond to simulated interactions in the crystal, in a grid of points that maps the whole crystal volume. This data base is called AGATA

Figure 2.3: Configuration of AGATA during the first commissioning experiment. Each crystal is labeled with its position code.

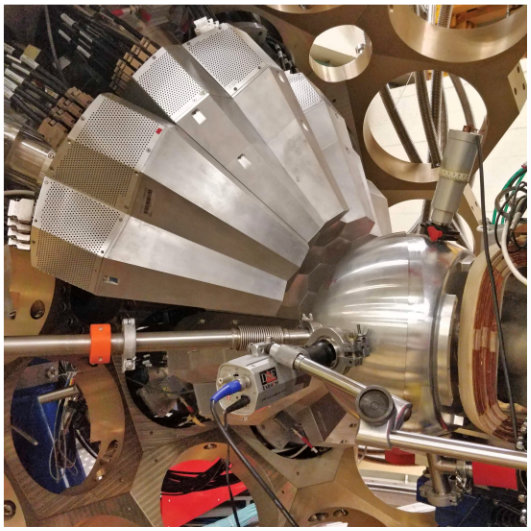

Figure 2.4: Photo of the closed reaction chamber with AGATA placed in the nominal position. The incoming beam enters from the left.

detector library (ADL) or also basis [20]. The position of the interaction is assigned according to the simulated pulses that fit best the measured signal. The information on the deposited energy and time of the interaction is also assigned accordingly to each point [21].

When energy is deposited in one segment, electrons and holes are collected, resulting in integrated charge signals of opposite signs at the two electrodes of the segment where the interaction occured. In the neighbouring segments induced transient signals are produced, for which the total collected charge is zero. Figure 2.5 shows an example of the shape of the net charge signal and the transient signal in the neighbouring segments with respect to the interaction. Thanks to the analysis of both net charge and transient signals it is possible to resolve the interaction position better than the segment size, with a precision of a few millimeters [22].

Among the different PSA algorithms that were developed, in this work the standard one was used, the Adaptive Grid Search [23]. This algorithm compares in two steps the measured signals with the calculated signals from a grid of points in the crystal. The first three dimensional search spans a coarse grid of 6 mm to find an approximate value of the interaction position and then a finer search with a grid of 2 mm is repeated around the found point. The search for the best correspondence of measured and simulated signals is done by minimizing the following figure of merit (FoM) [24]:

$$FoM = \sum_{j,t_i} |A_{j,m}(t_i) - A_{j,s}(t_i)|^p \tag{2.1}$$

$A_{j,m}(t_i)$ and $A_{j,s}(t_i)$ are respectively the measured and simulated signals in a segment j at the time t_i. The exponent p is a chosen positive number [24].

The good quality of the PSA performance is essential for a good reconstruction of the trajectories

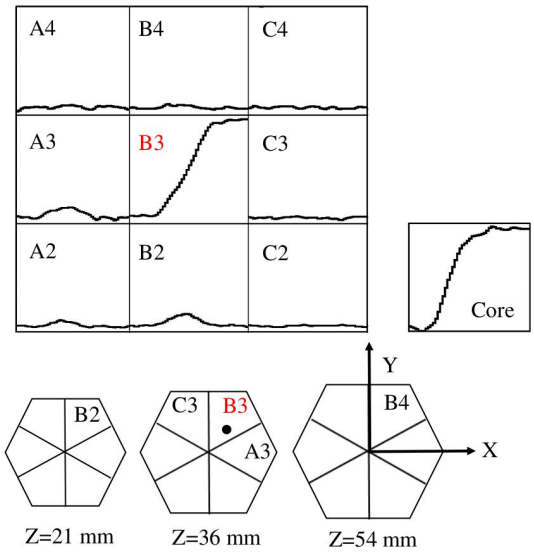

Figure 2.5: Net charge and transient signals for an interaction in an AGATA detector. The net charges are collected in the core and in segment B3, where the interaction occured (displayed with a black dot). In the neighbouring segments transient signals are induced and they are used to locate the interaction within the segment. Taken from ref. [21]

of the γ rays in the tracking algorithm. The pre-sorting of the data before the PSA is also important because the energy information needs to be well calibrated and the time signals need to be correctly aligned, as well as the cross-talk phenomenon between channels should be corrected. Moreover, the output information of the PSA is used to correct the effects of the damage to the germanium crystal lattice by fast neutrons in the following stage of the data processing [21].

2.2.5 Tracking algorithm

Thanks to the PSA, each interaction in the detector is analyzed and information on the deposited energy, time and position of the hit is extracted accurately. However, only a fraction the interactions give complete information about the original energy of the incident γ ray.

This is due to the fact that photon interaction in a medium can happen through different processes: mainly photoelectric absorption, Compton scattering and pair production. In particular, with a photoelectric absorption, all the energy of the photon is released in one hit, and an event like this contributes to the photopeak in an energy spectrum. In case a Compton scattering occurs, instead, the photon scatters on one of the electrons in the medium, releasing part of its energy and deviating from the original direction. After this interaction, the photon at lower energy can undergo further scatterings and usually is absorbed with a final photoelectric interaction. A partial energy deposit of one Compton-scattering γ ray in a segment of the detector populates the so-called Compton continuum in an energy spectrum, which contributes to the background for γ-ray spectroscopy.

Furthermore, the cross section of each of the interaction processes has a strong dependence on

the energy of the photon, as shown in fig. 2.6. The γ-ray energy range is from tens of keV to several MeV and, while for low-energy γ rays the dominant process is one single photoelectric absorption, for the photons beyond hundreds of keV the typical energy transfer happens through multiple Compton scatterings and a final photoelectric absorption. Therefore, for most of the γ-ray energies relevant for the spectroscopic analysis that AGATA is mainly used for ($\sim$ 100 keV - 10 MeV), the most common interaction process is the Compton scattering, which means that a large fraction of the interactions in the detector will not carry the information on the total energy of the γ ray.

The purpose of γ-ray tracking is using the information obtained by the PSA on the individual hits in the detector volume to reconstruct the trajectory of the photon in the medium and put together the partial energy deposits to recover the full energy of the incident photon, increasing the absolute photopeak efficiency and the peak-to-total ratio. Therefore, the tracking algorithm addresses mainly the Compton scattering photons in order to reconstruct the total energy of the photopeak.

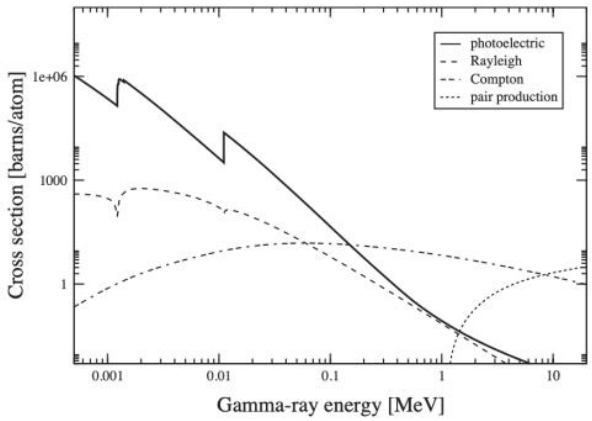

Figure 2.6: Cross sections of different interaction processes of photons in matter at changing incident energy.

Tracking algorithms can be divided into back-tracking and forward-tracking [25]. The feature of back-tracking algorithms is to start to reconstruct the track from the final photoelectric interaction, expected in a fixed energy range of 100-200 keV. However, the algorithm used in this work is the Orsay Forward Tracking (OFT), which belongs to the second category.

The forward tracking algorithms, instead, aim at identifying the first-interaction point of each photon. This procedure starts from the calculations of the angular coordinates (θ, ϕ) of all the interaction points in the array in a considered event. For couples of interaction points, their angular separation is computed, and if this is below a threshold α, the two interactions are grouped in the same cluster. This clusterization procedure is repeated for different thresholds α in the range from 0.15 to 1 rad in order to obtain different groupings. For each cluster, the interaction energies of the points are summed to give E_{tot}.

Starting from the source point, which is taken as the target position considering the current

AGATA position (nominal or close-up), a first interaction point i is considered and another j is taken as second within the same cluster. The energy after the first scattering is $E_{s,e} = E_{tot} - e(i)$ and before the scattering the energy is $E_t = E_{tot}$. Following the Compton formula, the remaining energy after the scattering i should be

$$E_{s,p} = \frac{E_t}{1 + \frac{E_t}{m_e c^2}(1 - \cos\theta_p)} \tag{2.2}$$

with θ_p as the angle between the incoming direction before the scattering i and the segment from i to j. After this, a figure of merit the is computed with the formula

$$F_E = \exp\left\{-2\frac{(E_{s,p} - E_{s,e})^2}{\sigma_e^2}\right\} \tag{2.3}$$

where σ_e is the uncertainty in the determination of the scattered energies due to position uncertainties of the interaction points. This is to quantify the goodness of point i as first interaction point.

For just two interaction points in the cluster, the score to evaluate the goodness of the cluster is

$$F_{s\to i\to j} = P(E_t)_{Comp} P(r_{s\to i}) P(E_{s,e})_{Photo} P(r_{i\to j}) F_E \tag{2.4}$$

where the $P(E)_{Comp/Photo}$ refer to the probability of Compton/photoelectric interaction at the given incoming energy, while $P(r)$ refers to the probability of propagation in the material on the r trajectory.

For larger clusters, an analogous calculation is done recursively for each interaction point, using each possible permutation of points for the scattering sequence.

The chosen sequence for the cluster is the one that maximizes the following figure of merit

$$F_{tot} = (F_{s\to i\to\ldots\to k})^{1/(2n-1)} \tag{2.5}$$

with n as the number of interaction points in the cluster, which goes from 2 to 6 [25]. After repeating the calculation for all the clusters, these are ordered by decreasing figure of merit, making sure that an interaction point cannot belong to multiple clusters and setting a lower threshold for the acceptance of a cluster. The remaining single interactions can be taken as clusters themselves.

The OFT code relies on the tuning of 3 parameters that determine the performance of the tracking according to the requirements of the experiment. These parameters are:

- **MinProbTrack** ($min_{P_{track}}$)- This defines a minimum probability threshold for the acceptance of the figure of merit from the tracking algorithm.

- **SigmaTheta** (σ_θ)- This quantifies the position resolution of the interaction points
- **Clustering Angle Reduction Factor** (*ClAngRed*) - This reduces by an additional factor the maximum clustering angle, which is already scaled by the total number of interaction points in the event.

The parameter **MinProbSing** which established a threshold for the acceptance of single interactions, that was previously tunable in the code [25], has been removed and now the single interactions are accepted on the basis of their range in Ge. In section 4.3, the optimization of these parameters to increase the performances will be shown.

2.3 PRISMA

PRISMA [11, 26] is a large acceptance magnetic spectrometer for the detection of low-energy medium-mass reaction products (5-20 MeV/A) in heavy-ion collisions around the Coulomb barrier.

Since the purpose of PRISMA is to analyze the reaction products recoiling from the target, it is placed after the reaction chamber with an angle that can be varied with respect to the beam line, as shown in fig. 2.7.

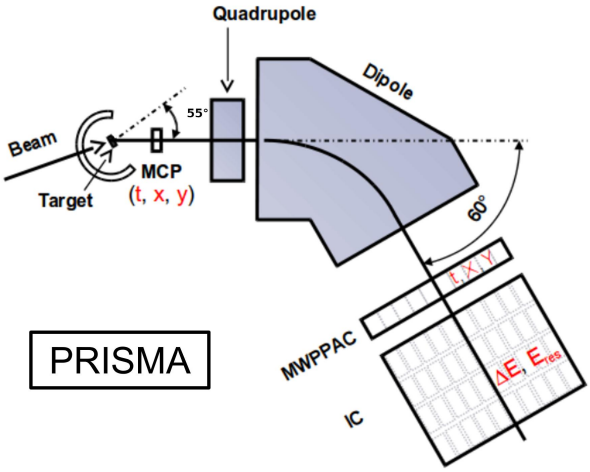

Figure 2.7: Scheme of the PRISMA spectrometer.

The spectrometer is made of three separate detectors and two optical elements. The front detector is an Micro-Channel Plate (MCP) detector that gives high-precision spatial and timing resolution for the fragments exiting the reaction chamber. Them, the ejectiles go through a magnetic quadrupole to be focused in the y direction and de-focused in the x axis and a large magnetic dipole to achieve spatial separation depending on the magnetic rigidity $B\rho$, which is proportional to Av/q, being A the mass number, v the velocity and q the charge state of the ion. After a drift in a vacuum chamber, a Multi-Wire Parallel-Plate Avalanche Chamber (MWPPAC) to measure the x and y position and the timing of the ions. Right behind the MWPPAC, a segmented ionization chamber is used to stop the nuclei and extract the stopping

power and energy information. In the following paragraphs, a more detailed description of the detectors is given.

2.3.1 MCP

The entrance MCP detector [27] is a rectangular (80×100 mm^2) position-sensitive and fast timing detector. The scheme is shown in fig. 2.8. The detector is based on an electrostatic field to accelerate secondary electrons emitted from a thin carbon foil ($\sim$ 20 μg/cm^2) when charged ions pass through it. A magnetic field parallel to the accelerating electric field is used to preserve the position information. The position-sensitive anode is made of two orthogonal delay lines made of 100 μm gold-plated tungsten wires. The efficiency for the detection of heavy ions is close to 100% and the spatial resolution in both x and y is around 1 mm. The time resolution is $\sim$400 ps. In the setup, a cross-shaped mask is used to have reference points in order to calibrate the position obtained from the detector.

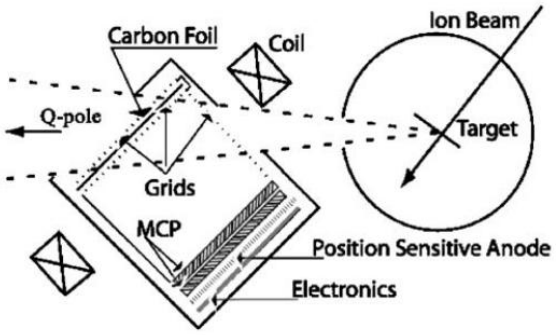

Figure 2.8: Scheme of the PRISMA MCP detector. From ref. [27]

2.3.2 MWPPAC

A measurement of the x and y position and timing of the ions is provided at the focal plane of PRISMA by the MWPPAC detector [26, 28]. This detector has a three-electrode structure: a central cathode and two wire planes for the x and y anodes, which are orthogonal with respect to each other. The wires are made of gold-plated tungsten with a diameter of 20 μm and they cover an area of 13×100 cm^2. Both the x anode plane and the cathode are segmented into 10 equal and independent horizontal sections of 10 cm of length, with vertical wires, while the y plane has horizontal wires. In the x and y planes, the spacing of the wires is 1 mm, while for the cathode is 0.3 mm. The detector has mylar input and exit windows and is filled with isobutane gas (C_4H_{10}) at a pressure of 7-8 mbar.

The OR of the cathode sections works as a trigger for the acquisition of PRISMA. The time information from the MWPPAC and the MCP are combined to obtain a measurement of the Time of Flight (ToF). A scheme of the detector can be seen in fig. 2.9

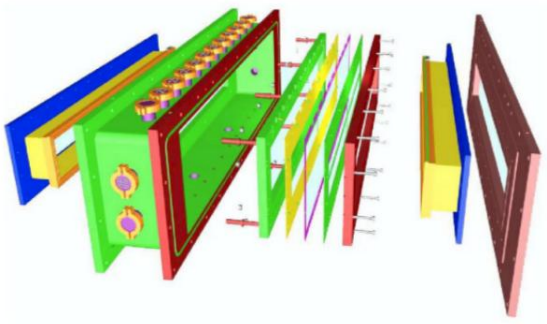

Figure 2.9: Scheme of the PRISMA MWPPAC detector. Taken from ref. [26].

2.3.3 Ionization chamber

Downstream from the MWPPAC, the PRISMA ionization chamber is composed of a $110 \times 20 \times 120$ cm^3 volume filled with either CF_4 or CH_4. Such large depth allows to use low gas pressure to stop the ions, which is up to 100 mbar. The electrodes of the IC are made of 40 pads: 10 horizontal sections as in the MWPPAC and 4 sections in the z directions (A,B,C,D), where each pad provides an independent ΔE measurement. Two side pads are present on the ends of each row to act as veto detectors for the trajectories that exit the detector. With each experiment, the pressure of the gas is optimized in order to have most of the ions of interest to stop between the C and D section of the IC. The total energy E of the ions is calculated by summing the partial energy loss in all of the sections, while the ΔE measurement is taken as the signal detected in the A or A+B sections. Thanks to the distribution of the ΔE and E of the measured ions, it is possible to achieve separation in the Z.

Chapter 3

Data Processing

The AGATA-PRISMA setup is a powerful tool for the study of nuclear structure with stable and exotic beams, where PRISMA allows the event-by-event full identification of the ejectile ions and AGATA detects the γ rays emitted by the produced nuclei.

In this chapter, the steps to treat the raw signals from this experimental setup until the full event characterization will be presented. Firstly, the data is processed separately for AGATA and PRISMA. Secondly, the data of both detectors is merged according to the timestamps. The correlation between the two detection systems, done with a time coincidence window, allows to perform γ-ray spectroscopy for a specific reaction channel given by the selection of A and Z in PRISMA. In this work, the focus will be mainly on AGATA, since this was my primary task, but a brief description of the PRISMA processing will follow.

3.1 AGATA data processing

In order to get to the final, tracked, global γ-energy spectra, the data processing of AGATA is divided into two stages: in the *local* level each crystal is treated independently, while in the *global* level events are built with the output of the local processing of all crystals and merged with the complementary detector data.

The acquisition and processing of the AGATA data flow are performed with NARVAL [29] using a chain of different actors. Each actor has a specific function to either read the data, process it or write it onto files. Femul is a NARVAL emulator to reprocess (replay) the data offline. More details about the data processing can be found in ref. [21].

The actors are divided into categories with different functions:

+ **Producers** - Read data from the electronics or disk.

+ **Intermediaries** - Receive the data from the previous step, perform operations on it and sends it to the following actor. Divided into:

- **Filters** - Process the data locally or globally.
- **Dispatchers** - Sends to the data on the local or global level to a builder or a merger.
- **Builders** - Builds the events from local to global level or merge the data with the complementary detectors data.

+ **Consumers** - Write the output data to files.

The chosen sequence of actors for the processing is called topology. The details of the actors in the topology that is used for the full pre-sorting of the AGATA data with PRISMA as complementary detector are illustrated in table 3.1.

Table 3.1: Topology of the NARVAL actors for the complete processing of the AGATA data with the merging of the processed PRISMA data.

Actor type	**Actor name**	**Function**
	From raw to PSA	
Producer	Crystal Producer	Reads data from the readout chain or from raw data files
Filter	Preprocessing Filter	Energy calibrations, cross-talk and dead segment corrections and local time alignment of the signals.
Filter	PSA Filter	Performs PSA and obtains energy, time and position information of every interaction.
Consumer	Basic AFC	Saves the output of the PSA on disk files (psa.adf)
	From PSA to ROOT Tree	
Producer	Basic AFP	Reads data from psa.adf files.
Filter	PostPSA Filter	Neutron damage correction, recalibration of the spectra and global time alignment.
Builder	Event Builder	Builds global events from the local outputs of the crystals based on timestamps.
Builder	Event Merger	Merges data from AGATA and PRISMA according to the timestamps. Already processed data from PRISMA is read with a Producer actor in advance.
Filter	Tracking Filter	Applies tracking algorithm to reconstruct the γ-ray trajectories in the array.
Consumer	Tree Builder	Saves all the variables relative to each event onto a ROOT Tree on the disk.

The topology in the table is divided into two chains: one goes from the raw data to the output of the PSA and the second one starts from the output of the PSA and reaches the filling of the

final output tree of variables. This separation exists because during the experiment, NARVAL performs the first steps of the processing until the PSA, saving on the disk directly the output of this in the AGATA Data Flow format (.adf) files, without recording all the signal traces. The writing of the traces may be activated from the acquisition settings, but usually it is neglected for a matter of memory optimization and in order to avoid dead time at high rates of acquisition. However, if a full offline replay needs to be performed (*e.g.* to change settings in the *Preprocessing Filter*), recording the traces is needed, in order to start from the raw data and repeat every step of the processing. Instead, the second part of the chain is executed offline, and uses the *psa.adf* files as input.

Due to this structure, the steps up to the PSA have to be optimized before the experiment. Instead, all the steps from the *PostPSA* on can be optimized offline and replays can be run directly from the PSA reduced files.

In order to set the optimal parameters for the filters, radioactive sources must be used to have reference peaks in the energy spectra. In particular, an acquisition run with a ^{60}Co source is needed for most of the parameter estimations and a run with ^{152}Eu is needed for the final energy calibration.

The summary of the actors in the data processing chain is shown also in fig. 3.1.

3.1.1 Local level processing

Crystal Producer

The first step of the processing is the *producer* actor, which decodes the binary data of the short traces and applies a trapezoidal filter in order to extract energy and time signals for the channels. In the testing phase of the online acquisition, the parameters of the trapezoidal filter as well as the ADC offset of the digitizer are optimized for each crystal. Although the gains of the preamplifiers are preliminarily adjusted to match, the spectra saved after the producer stage are not calibrated and they are used to evaluate an energy linear calibration with no offset, thanks to the two peaks of ^{60}Co.

In the processing, the software *TkT* is used for displaying and fitting energy or time spectra that are produced when running NARVAL of femul. In this section, when the spectra from all the segments are displayed together, they are taken from *TkT*, which displays them in a 6x6 grid for the 36 segments. The columns of the grid correspond to the radial sectors of the crystal (A-F), while the rows refer to the longitudinal segmentation (1-6), following the convention explained in section 2.2.1.

The 36 uncalibrated amplitude spectra of the operational crystals at the Producer stage are shown in fig. 3.2.

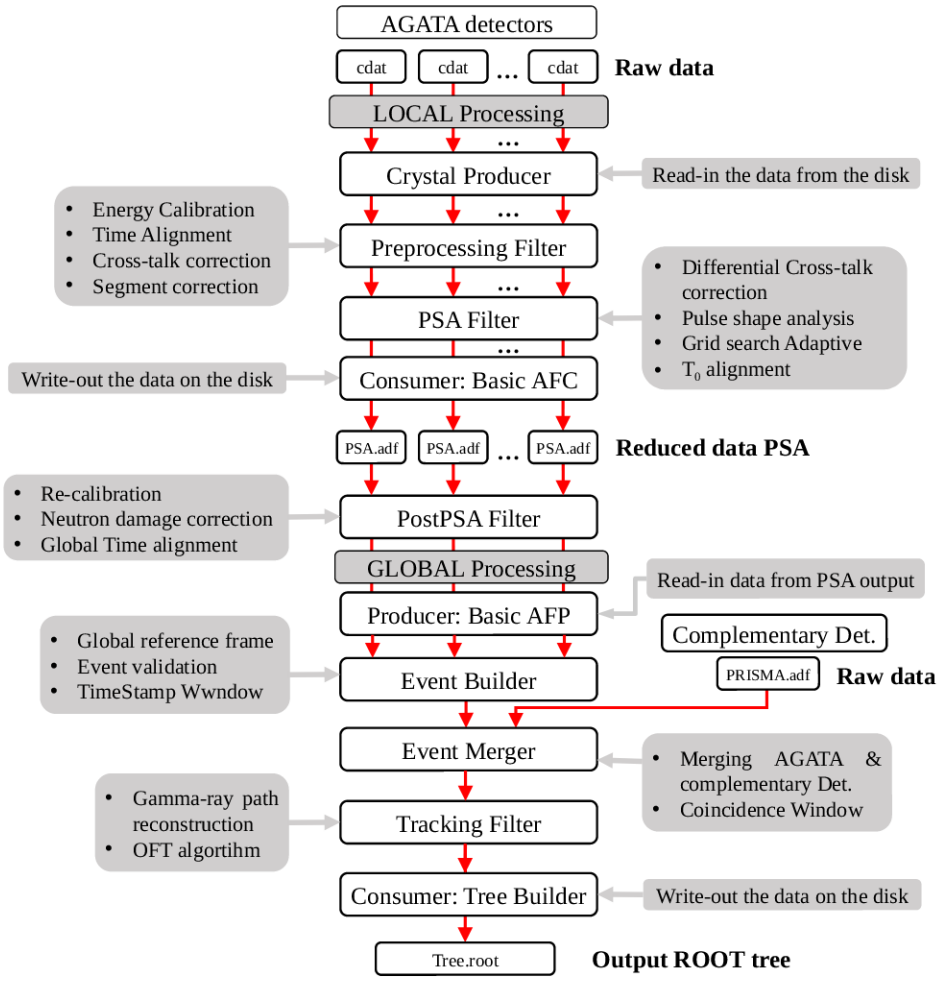

Figure 3.1: AGATA data processing scheme with the different NARVAL actors. Updated from the table in ref. [21].

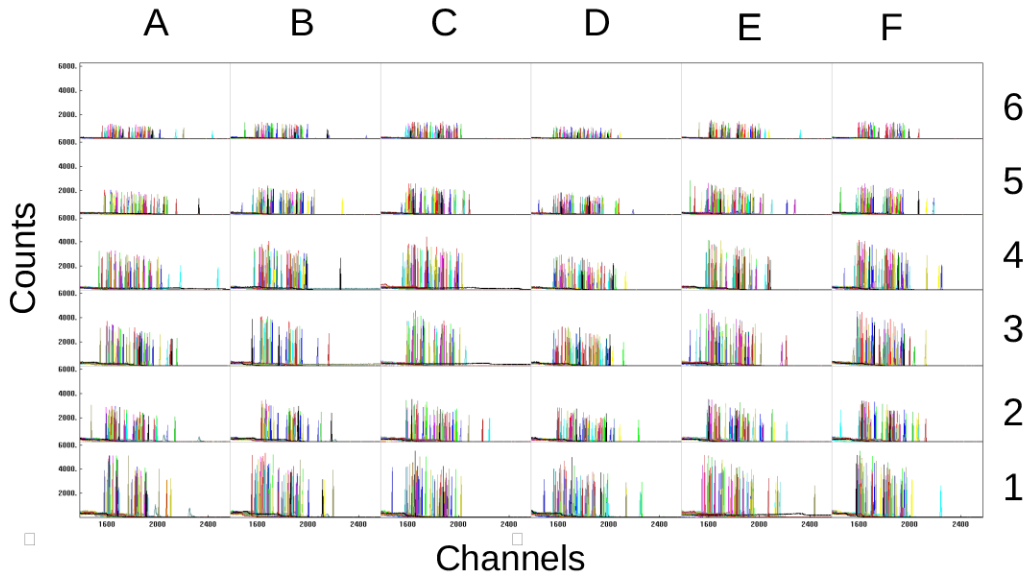

Figure 3.2: Segment spectra for ^{60}Co for all operational crystals (each with different colour) before energy calibration (at the Producer stage).

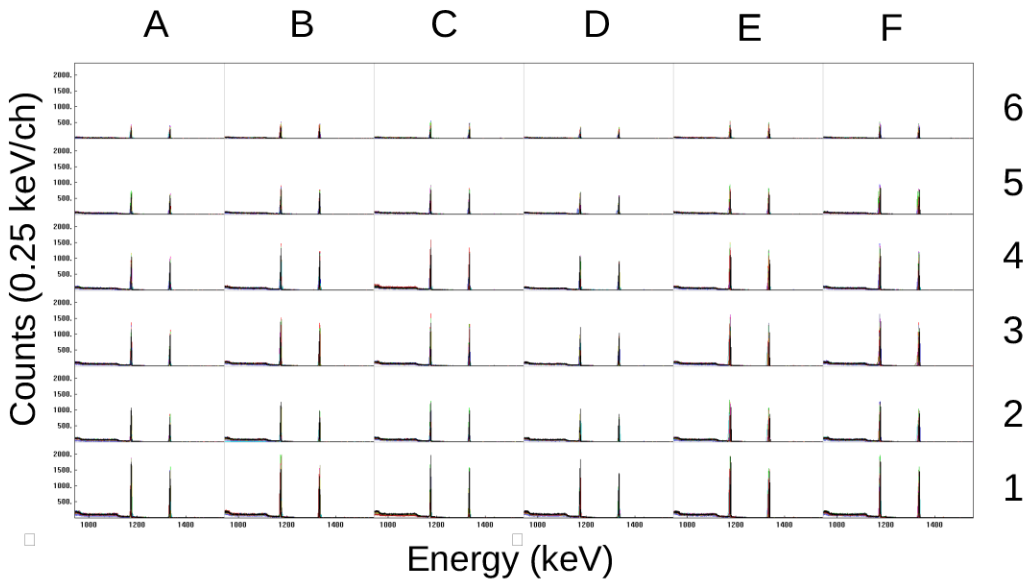

Figure 3.3: Segment spectra for ^{60}Co for all operational crystals (each with different colour) after energy calibration (at the Preprocessing stage).

Preprocessing

The *preprocessing* filter is then responsible for applying the necessary corrections for a good performance of the PSA algorithm. First, a linear energy calibration with no offset is performed for each segment and core signal. The calibration gains are evaluated from the positions of the two most intense peaks from a ^{60}Co source. The calibrated segment spectra at the preprocessing stage are shown in fig. 3.3. At this step, the calibration is done using the spectra recorded with a multiplicity of segments equal to 1 in order to avoid cross-talk effects.

Cross-talk is a phenomenon that appears in an electrically segmented detector when a single γ ray interacts and releases energy in multiple segments [30, 31]. The proportional cross-talk is seen with a signal amplitude loss, proportional to the neighbouring partial energy depositions. This translates to a shift in the centroid of the peak in the energy spectrum of the sum of the segments, which increases with the multiplicity of segments firing, as seen on the left plot in fig. 3.4.

Differential cross-talk, instead, is a distortion of the induced signal on other segments during the transient of the traces and it also needs to be corrected to properly perform the PSA.

Cross-talk is indeed the next thing to correct in the sorting of the data. In the *preprocessing* filter, cross-talk correction parameters are applied in order to correct the amplitude loss. The matrix that contains these parameters of interaction between segments is evaluated thanks to the use of the *xTalkSort* software [32] on data coming from a ^{60}Co source. Fig. 3.4 shows the spectra of the sum of the segments before and after the cross-talk correction, where the black histogram includes all multiplicities of segments, while the coloured ones are divided by the number of firing segments. After the cross-talk correction, right plot, the peaks for all multiplicities are

aligned and the global black peak is sharper and centered at the right energy.

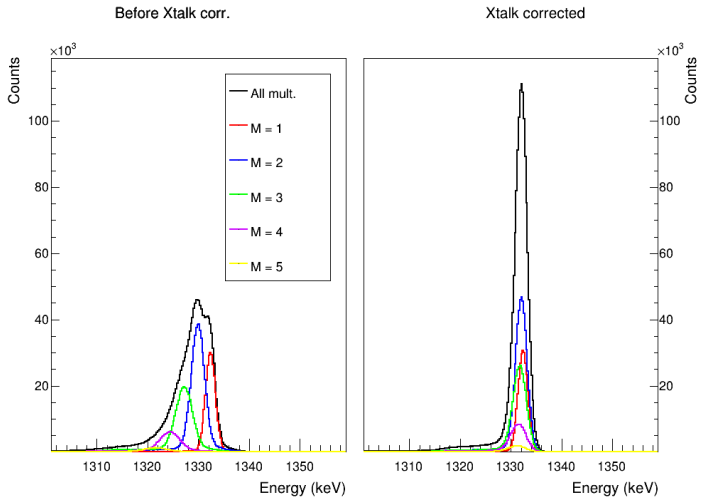

Figure 3.4: Spectra for the sum of the segments at different multiplicities before (left) and after (right) cross-talk corrections. The correction aligns the centroids of the peaks for different multiplicities, making the global peak (black) sharper and centered.

Sometimes the AGATA crystals can present segments with problems in their signals. Depending on the problem this segments can be classified as *dead* or *unstable* segments. When having one problematic segment, it is possible to recover the full performance of the crystal only if the rest of the segments are all working properly. *Dead* segments are divided into *lost* and *broken* segments. The first kind happens when the net charge is correctly collected by the segment but there is no information in the acquisition chain. This connects to an issue either in the warm part of the pre-amplifier or in the digitizer. *Broken* segments, instead, are related to an issue in the cold part of the preamplifier and in this case the charge is not collected properly and it flows to the neighbouring segments, producing ghost peaks in their spectra. *Unstable* segments show an energy gain that varies in time and can produce multiple peaks or broader peaks in the energy spectra.

The procedure for recovering a dead segment goes through the cross-talk matrix, where the energy of the sum of the segment is compared to the energy detected in the core. When properly functioning, the matrix should be populated close to the diagonal because we expect the two energies to match, but in the case of dead segments, the structure of this matrix deviates from the diagonal. An example of recovery of a dead segment is shown in fig. 3.5, where in crystal 00A segment C1 is recovered successfully. The procedure for the correction is explained in ref. [32].

In the new configuration at LNL, several ATCs were replaced or repaired with respect to the previous experimental campaign at GANIL [9]. At the first test of the detectors with radioactive sources, a number of issues were found with lost or unstable segments. The procedure requires to check the signals and apply the needed corrections before each experiment. Table 3.2 shows the issue with the channels in each crystal that were found during the testing of the new configuration at LNL before the commissioning experiment 2.1. Beyond the issues listed in table 3.2, crystal

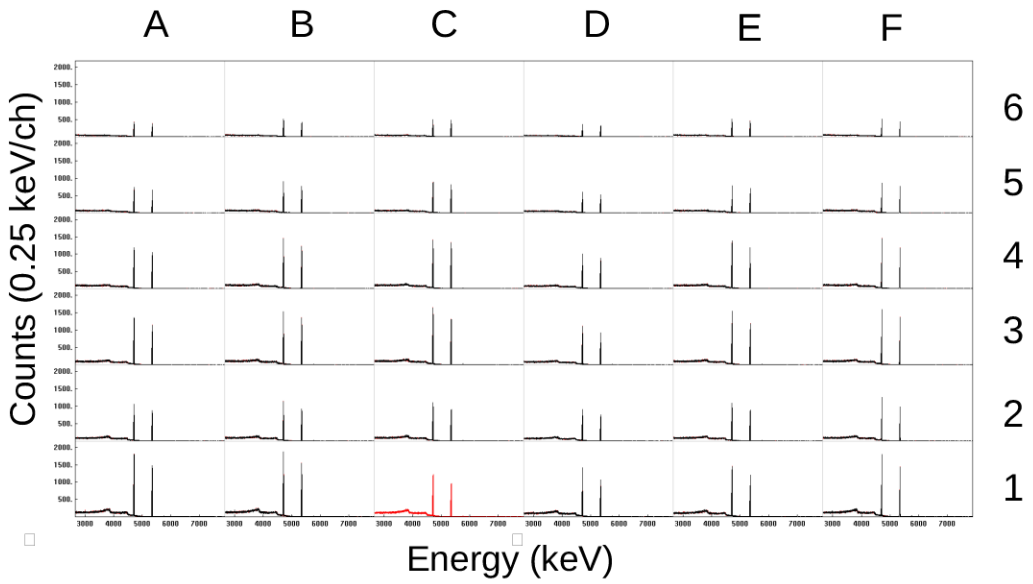

Figure 3.5: Example of lost segment in the crystal 00A. The black spectra are before cross-talk corrections and dead segment correction, while the red one is after the corrections. Segment C1 is a lost segment but after the correction it is recovered.

06B had problems with the high voltage and 09B could not be synchronized in the GTS, so they were both excluded from the acquisition system and no data was recorded for these two detectors.

Table 3.2: Channel issues found during the testing of the acquisition

Crys. N°	Issue	Outcome
00A	seg. C1 lost	recovered
01B	seg. A2 lost	recovered
02A	seg. E5 unstable	recovered as lost
02B	seg. A1 lost	recovered
06A	seg. B2 broken	could not recover
06C	noisy core	could not recover
07C	periodically noisy core	could not recover
08A	seg. B3 lost	recovered
08B	seg. A1-2,B1-2-3-4 unstable	could not recover
08C	seg. B1-2-3 lost	could not recover
10B	seg. D5 lost (mult. = 1)	could not recover
11A	seg. F1 lost	recovered

Another step in the *preprocessing* filter is the time alignment. First, it is needed to synchronize the signals from the segments to the core that is triggering, calculating shift parameters. The second step is to align the cores of the different crystals modifying the T_0 parameter. This reference time refers to the offset of the core signal of each crystal with respect to the simulated

traces coming from the data base for the PSA. Figure 3.6 shows the time difference spectra of all the segments with respect to the core in crystal 00A after the local time alignment. Figure 3.7 shows the alignment of the T_0 parameter in the cores of the operational crystals. The T_0 alignment affects the reconstruction of the hit position by the Pulse Shape Analysis algorithm.

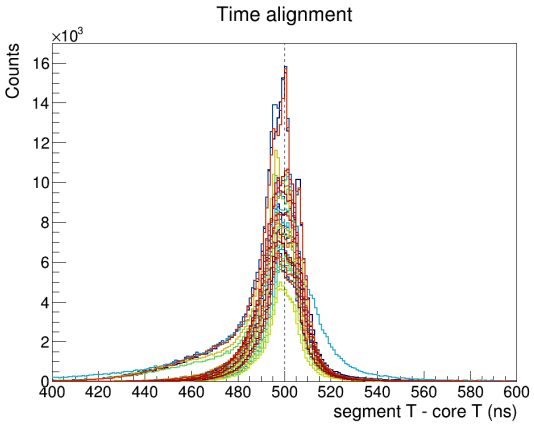

Figure 3.6: Time difference spectra of segments of crystal 00A after local time alignment.

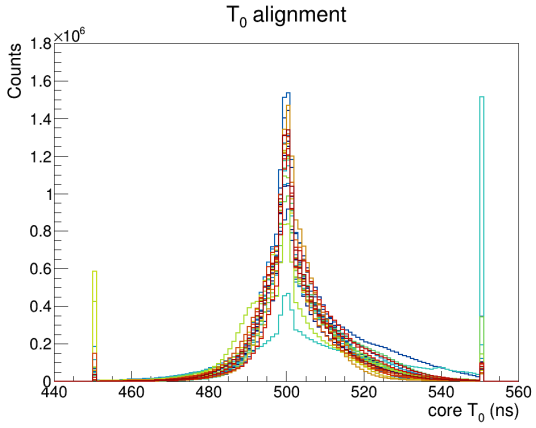

Figure 3.7: Core *Tzero* spectra for the operational crystals after alignment.

PSA

The next actor in the chain is the *PSA* Filter, which performs the Pulse Shape Analysis algorithm. The purpose of this process is to compare the acquired traces of each segment during one interaction with a simulated data base of interactions that maps the whole germanium crystal. The interaction position of the γ ray is found by minimizing the figure of merit that compared the experimental and the simulated traces (section 2.2.4). Figure 3.8 shows the traces in the segments and core comparing the measured signal (red) and the matching simulated one (blue). There are several minimization algorithms for the localization of the best position and in this case the Adaptive Grid Search was used [23]. The information on the energy, time and position of each interaction is then used in the tracking algorithm. It is possible then to map the interactions of the γ rays in one crystal by their position, like in fig. 3.9. The fact that the hits are concentrated in the layer of the germanium that is facing the scattering chamber, *i.e.* the more narrow, is consistent with the absorption length of photons in the material, which for 1 MeV γ rays is 3.8 cm.

PostPSA

The *PostPSA* Filter is the following step of the processing, which implements a set of corrections and refinements.

In the course of experiments, fast neutrons are produced in different types of reactions. The irradiation of the germanium crystals by fluxes of fast neutrons produces defects in the semiconductor lattice structure, which act as traps for charge carriers. This effect causes the charge collection at the electrodes to be partial and therefore the signal amplitude can be lower with

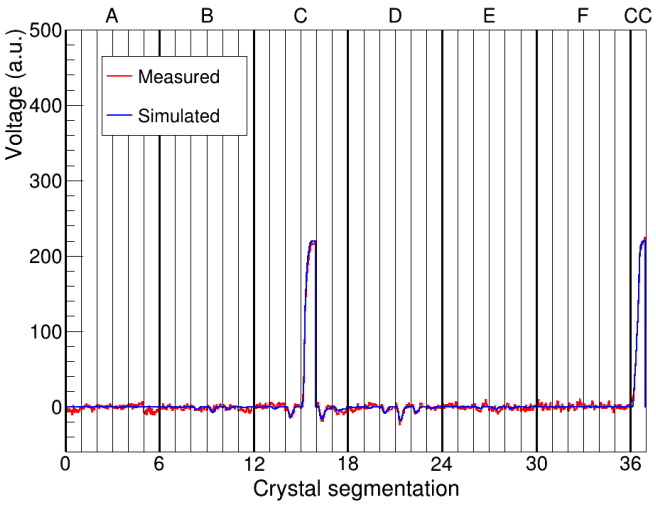

Figure 3.8: Comparison of the short traces acquired in each segment and the simulated ones in the reference data base for one interaction in crystal 11B. The label CC corresponds to the core signal.

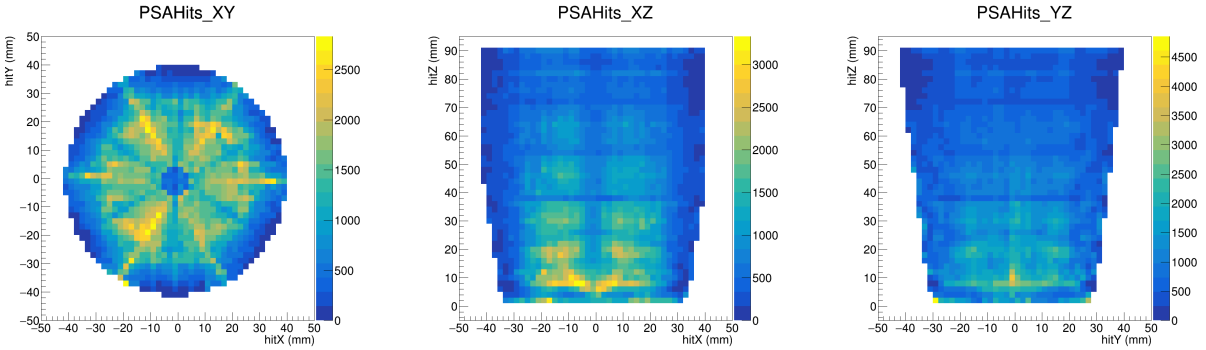

(a) X-Y hit distribution (b) X-Z hit distribution (c) Y-Z hit distribution

Figure 3.9: Hit distribution in crystal 00A coming from the Pulse Shape Analysis algorithm,

respect to the energy released in the interaction. Being the AGATA crystals n-type HPGe detectors, the defects in the lattice caused by neutron irradiation trap more efficiently holes as charge carriers, which means that the effect is seen more significantly in the signals from the segments [1]. In the energy spectra, this behaviour produces a low-energy tail on the γ-ray peaks, that implies a worse energy resolution (see example in fig. 3.10)

The lattice damage can be recovered by the annealing of the crystals, but it is impractical to apply this procedure after every experiment. However, thanks to the high position resolution of the interaction points obtained with the PSA algorithm, it is possible to correct for the trapping effects in the processing [33]. Since the charge carriers collection efficiency depends on the position in the crystal and on the travel path to the electrode, it is possible to estimate a set of correction parameters for electrons and holes based on the PSA hits. This is summarized in the *Trapping.cal* configuration files that are taken into account in the *PostPSA* stage of the processing [32]. The correction using the trapping files allows to reconstruct the original γ

energy considering the fraction of charge that was not collected, therefore the corrected peak has a sharper shape and the left tail has partially disappeared, as it is shown in fig. 3.10.

In the configuration of the first commissioning, neutron damage was observed on five crystals: 08A, 08B, 08C, 11A and 11B. Table 3.3 shows the effect of the correction on the width of the peaks. In particular, the procedure improves significantly the resolution for the sum of the segments, while for the core spectra the effect is not very important in most cases. In the case of 08A, 08C, 11A the core correction was disabled because there was no improvement in energy resolution.

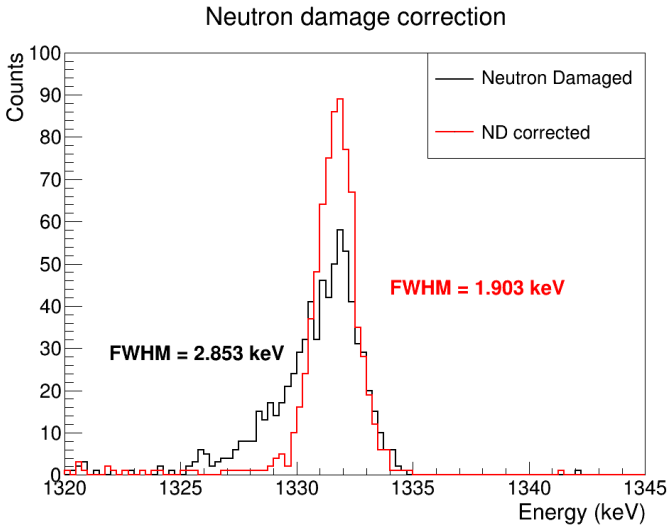

Figure 3.10: Example of neutron damage correction in one of the affected detectors (11B, seg. F4). The peak after the correction shows a smaller FWHM and a more symmetric shape.

Table 3.3: FWHM of the 1.3 MeV peak of ^{60}Co before and after neutron damage correction for the damaged crystals.

	Sum of segments		Core	
FWHM (keV)	before NDC	after NDC	before NDC	after NDC
08A*	3.260	2.877	-	2.769
08B	3.611	2.946	2.490	2.484
08C*	3.456	3.168	-	2.726
11A*	3.340	3.086	-	2.607
11B	5.108	3.931	2.980	2.908

* The correction for the electron trapping (core) was disabled because it did not bring to an improvement in the resolution.

At this stage, the data files have two sets of 36 spectra: one type is made with the signals from the segments directly, while the second one is composed by partial spectra acquired by the core, each one in coincidence with one specific segment. For each crystal it is possible to select an option called *ForceSegmentsToCore*, which is used to renormalize the sum energy of all segments to the energy measured in the core. With this option, the spectrum of the sum of the segments that is sent to tracking looks equal to the core spectrum.

This procedure is convenient when the resolution of the core is better than the one of the sum of the segments. Table 3.4 shows the widths of the reference 1.3 MeV peak of the ^{60}Co source for each crystal considering the spectrum of the core or the sum of the segments. On average, the core resolutions are better, so the option *ForceSegmentsToCore* was applied to all operational crystals. This choice was also justified by the observation that the calibration that was performed before the experiment proved to be more stable for the cores during the experiment, while the spectra of the segments showed some drifts in the gain, therefore all final spectra include the option *ForceSegmentsToCore*.

Additionally, crystals 06C and 07C were problematic. Crystal 06C was not biased fully during the experiment, while 07C had a periodic shift in the baseline of the core, which was associated with significant noise that caused a large broadening of the peaks. Therefore, these two crystals were also excluded from the topology for the later replays.

After the neutron damage correction and applying the *ForceSegmentsToCore* option, a recalibration is applied to all segments and afterwards to the sum of segments and to the core in different steps. This time, the calibration function is a linear one with an offset and is evaluated with ten peaks of a ^{152}Eu source, spanning a wider energy range (120 to 1400 keV). The last column of table 3.4 shows the FWHM of the 1.3 MeV peak of ^{60}Co after all the steps in the PostPSA.

The last step before sending the events to the builder is a global time alignment, which matches the different offsets in the timestamps of the crystals, synchronizing all the timings. Figure 3.11 shows the time difference spectra between the core of crystal 00C and the rest of the active crystals before and after the global time alignment.

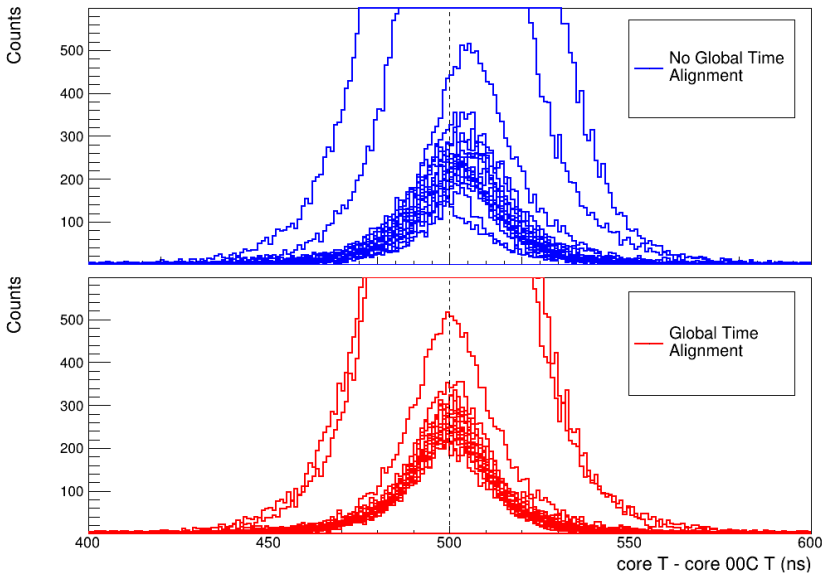

Figure 3.11: Time difference spectra of crystal 00C with respect to the other crystal before and after global time alignment.

Table 3.4: FWHM of the 1.3 MeV peak for core, sum of segments and final spectrum after all PostPSA correction for all crystals.

Crystal	Core FWHM (keV)	SumSeg FWHM (keV)	Final FWHM (keV)
00A	2.75	2.73	2.75
00B	2.85	2.77	2.85
00C	2.71	2.69	2.71
01A	2.54	2.59	2.55
01B	2.57	2.45	2.57
01C	2.57	2.51	2.57
02A	2.40	2.69	2.40
02B	2.48	2.63	2.48
02C	2.74	2.81	2.74
06A	2.52	2.77	2.52
07A	2.52	2.76	2.52
07B	2.74	2.58	2.74
08A	2.77	2.88	2.78
08B	2.48	2.95	2.49
08C	2.73	3.17	2.73
09A	2.56	2.68	2.56
09C	2.54	2.86	2.54
10A	2.38	2.66	2.38
10B	2.48	3.12	2.48
10C	2.38	3.09	2.38
11A	2.61	3.01	2.61
11B	2.99	3.93	2.99
11C	2.85	4.89	2.85
Average	2.62	2.92	2.62

3.1.2 Global level processing

Event Builder and Merger

The information from the single crystals collected in the local level needs to be put together and merged with the signals from complementary setups for coincidence measurements.

The first actor in this stage is the *Event Builder*, which combines interactions in different crystals into one single event. The events were constructed within a time window of 0.5 μs. In the building stage, the interaction points coming from PSA are also translated in the global reference frame thanks to a mapping of the ATCs. The distribution of the hits in the global frame of reference is shown in fig. 3.12a and compared with the front view of the array in the photo of fig. 3.12b

Next, the γ events are merged with the information from the complementary detectors, *i.e.* PRISMA in the first commissioning experiment, within a coincidence window of 2.5 μs.

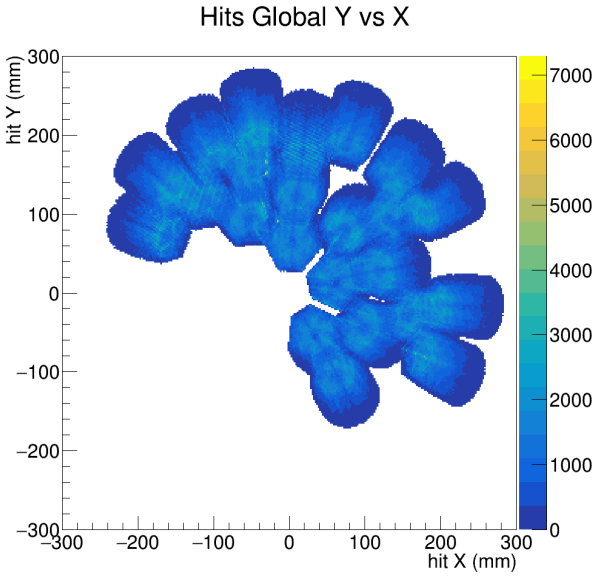

(a) X-Y hit distribution in the global frame

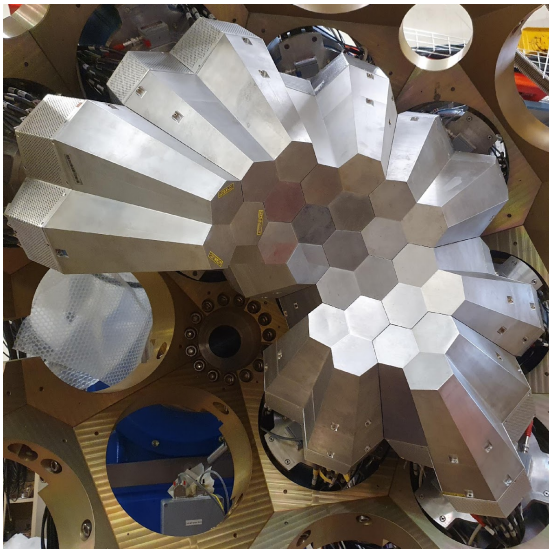

(b) Front view of AGATA with the configuration in the commissioning

Figure 3.12: Comparison between the hits in the global frame coming from the PSA and the real configuration of AGATA. The detectors that were excluded from the analysis (06B, 06C, 07C, 09B) do not appear in the left plot.

Tracking

The tracking is performed in the replay in the Merger stage. By specifying a set of parameters it is possible to tune the algorithm on one particular γ-ray energy or to optimize one characteristic in the final spectra, such as total efficiency or peak-to-total ratio. The parameters chosen in this work were optimized for the 1.3 MeV peak of ^{60}Co and the procedure will be shown in section 4.3. The increase in efficiency given by the tracking can be read in table 3.5, where the integral and peak-to-total of the 1.3 MeV peak of ^{60}Co is compared between the two spectra, and there is a significant increase in these two values. The FWHM, on the other hand, increases as a result of the reconstruction of the photo-peak events. The tracked spectrum and the core spectrum from a ^{152}Eu source are compared in fig. 3.13. From the plot, it is visible how after the tracking algorithm the Compton background is significantly reduced at lower energies and the height of the peaks at higher energies is increased, meaning an improvement of the peak-to-total ratio.

Table 3.5: Characteristics of the 1.3 MeV peak of a ^{60}Co source before and after the tracking algorithm. The P/T is calculated as in eq. 4.1

	FWHM (keV)	Efficiency (%)	P/T (%)
Core	2.767(2)	2.52(7)	17.383(12)
Tracked	2.918(2)	3.24(9)	30.328(19)

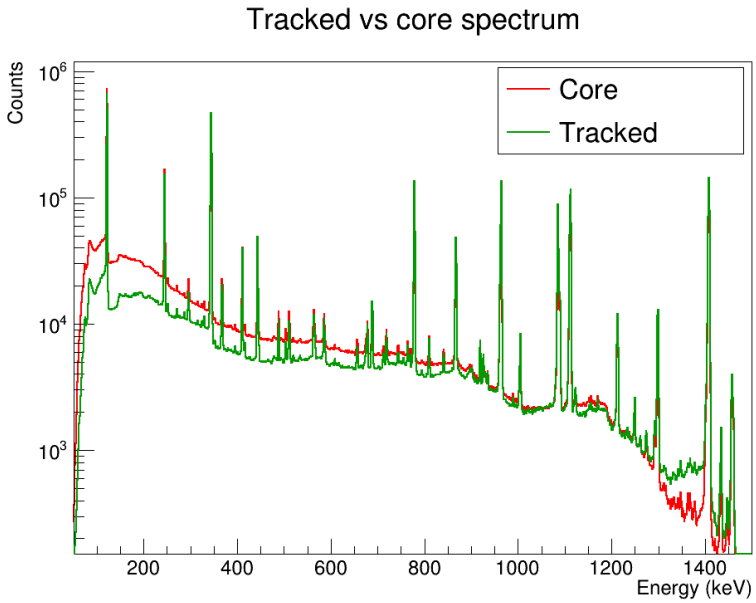

Figure 3.13: Comparison of the core spectrum and the tracked spectrum for a ^{152}Eu source.

3.2 PRISMA data processing

As explained in section 2.3, the PRISMA spectrometer is composed by three different parts, an entrance MCP, a focal plane MWPPAC and a segmented ionization chamber. Combining all the information coming from the three detectors, it is possible to obtain the full characterization of the recoiling nucleus in the reaction that enters the spectrometer: the A and Z, which constrain the investigation to one single reaction channel, and the ejectile $\vec{\beta}$, vector, which is essential for the Doppler correction of the γ rays detected in AGATA.

The presorting of PRISMA [26, 34] data goes through calibrations for each of the involved detectors. In contrast with AGATA, the evaluation of the calibration parameters cannot be done without beam, so this phase was performed directly with the experimental data. For the commissioning experiment most of the work on the processing of PRISMA was performed and described in ref. [35].

The first step is to calibrate in position the signals of the MCP and MWPPAC. The MCP has a metal mask in front of the emissive foil that gives reference points in order to perform a transformation of the acquired X and y signals to match the known positions. Regarding the focal plane MWPPAC, each of the section gives a *left* and a *right* signal, and the actual position x_{FP} is taken as the difference between right and left and then calibrated in millimeters.

The MWPPAC acts also as the start signal for the ToF measurement, while the delayed time signal of the MCP gives the stop. The sections of the focal plane detector therefore need a time alignment among them to be used all together.

The ionization chamber pads also need a calibration, which is not actually a conversion from ADC units to MeV, but it is a process of gain matching between the different sections. This is

performed before the experiment by using a pulser that inputs a known charge in each channel, from which the adjustment gain is extracted for each part of the IC. In addition to this, the events where the side pads have fired get rejected.

3.2.1 Trajectory reconstruction

After the pre-sorting and calibration of the detectors composing PRISMA, all the information regarding each detected event is used to reconstruct the trajectory of the ejectile ion and extract essential quantities to identify the charge and mass of the particle. The calculation is done starting from the detected position at the entrance, from the MCP, and at the focal plane, from the MWPPAC, along with the knowledge of the magnetic field intensity in the quadrupole and dipole magnets. The trajectory is assumed to start at the center of the target in order to calculate the entrance direction. Using with the equations of motion of a charged particle in a magnetic field it is possible to estimate the trajectory and especially the magnetic rigidity in the dipole magnet $B\rho$ [26]. During the reconstruction, the trajectory is assumed planar in the horizontal plane.

In the quadrupole magnet, the magnetic field is given by

$$\vec{B} = -\nabla U(x,y) \quad \text{where} \quad U(x,y) = \frac{B_{max}}{R}xy \tag{3.1}$$

In this equation, x and y are respectively the horizontal and vertical coordinate, B_{max} is the maximum intensity of the magnetic field and R the inner radius of the quadrupole magnet. The Lorentz force governs the motion of the particle in the magnetic field:

$$\vec{F} = q\vec{v} \times \vec{B} \tag{3.2}$$

Solving the equation 3.2 for the magnetic field 3.1, the obtained path is a hyperbolic motion inside the quadrupole that defocuses ions in the horizontal plane and focuses them on the vertical one [36]. The exit coordinates from the quadrupole are consequently calculated. The products then enter the dipole magnet, which has a uniform magnetic field oriented in the vertical direction. The trajectories of the ions inside this field will be characterized by a uniform circular motion of radius ρ with the following relation for the magnetic rigidity:

$$B\rho = \frac{p}{q} \tag{3.3}$$

After the dipole, the motion is in a straight line until the focal plane detector, where the position of the ion is measured.

The reconstruction of the trajectory exploits the fact that once the entrance position and direction is known, from the MCP, then the magnetic rigidity inside the dipole $B\rho$ determines uniquely the path of the particles inside the spectrometer. This means that given a value of $B\rho$, the final position of the ion at the focal plane detector can be calculated. With the minimization

of the distance between the calculated position and the measured one with the MWPPAC, the proper value of $B\rho$ is extracted and the total length of the particle path L from the MCP to the MWPPAC is calculated from the complete reconstructed trajectory.

At this point, the calculation of the β of the particle is performed:

$$\beta = \frac{L}{ToF \cdot c} \tag{3.4}$$

Then, with eq. 3.3 and the relativistic expression for the momentum $p = mv/\sqrt{1-\beta^2}$:

$$\frac{A}{q} = \frac{B\rho}{\beta} \cdot \sqrt{1-\beta^2} \cdot const \tag{3.5}$$

In the commissioning experiment, the average β of the ejected ^{32}S ions is around ~ 0.09, which means that $\sqrt{1-\beta^2} \sim 0.996$, and can be approximated as 1. Therefore, the expression for the A/q ratio becomes:

$$\frac{A}{q} = \frac{B\rho}{L} \cdot ToF \cdot const \tag{3.6}$$

3.2.2 Channel selection

From the ionization chamber, the $\Delta E - E$ matrix is built, where on the vertical axis the energy deposit in the first two IC layers (A and B) is displayed, while on the horizontal one, the total energy deposition. This plot allows to see some band structures that represent a separation in the atomic number of the ions. The Z selection in the commissioning experiment is shown in fig. 3.14, with the most intense Z channel being the $Z = 16$, which is the same atomic number as the beam. A fraction of these events come, for example, from quasi-elastic reactions. The next step is to create graphical cuts on top of this matrix in order to sort the events depending on their Z, which is assigned starting from the elastic channel ($Z = 16$ in the commissioning experiment) being the most populated one.

After the Z selection, the charge states q need to be identified as well. This procedure is done on the E *vs.* $\rho\beta$ matrix (ρ being the curvature radius in the dipole magnet) for each Z, where different charge states appear on different diagonal structures. Graphical cuts are done on this matrix as well, and compared with simulations for determining the most intense charge state and assigning the rest of them accordingly. The q selection relative to $Z = 14$ is shown in fig. 3.15.

With a gate in Z and q, the A/q spectrum can be obtained from the trajectory reconstruction and can be multiplied by q to obtain the mass number of the ion. This process involves an offset in the A/q that allows the final values to be centered around calibrated A values. The global mass spectrum with a gate in Z comes from the sum of all the A/q spectrum gated in Z and q, multiplied by the corresponding q. The mass spectrum for $Z = 14$ is shown in fig. 3.16.

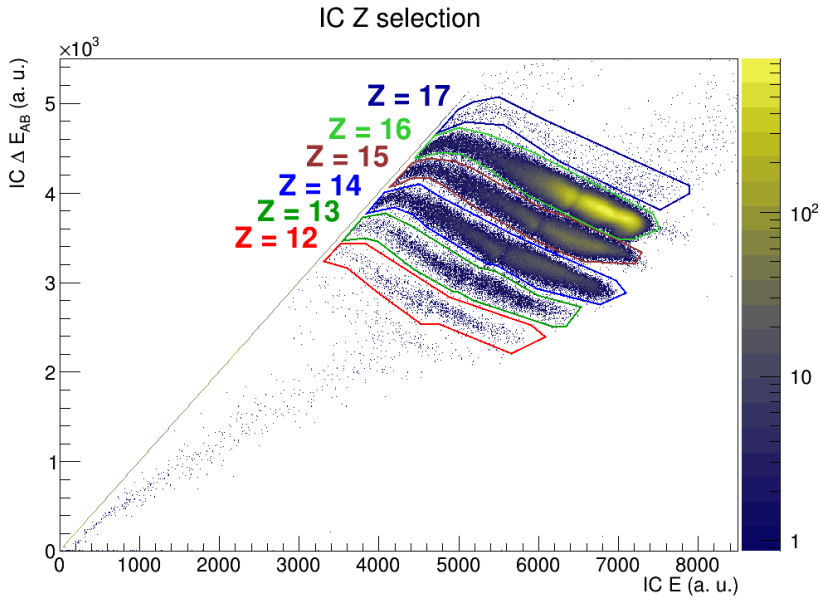

Figure 3.14: $\Delta E - E$ matrix from PRISMA ionization chamber. The displayed cuts allow the selection on the Z of the ions.

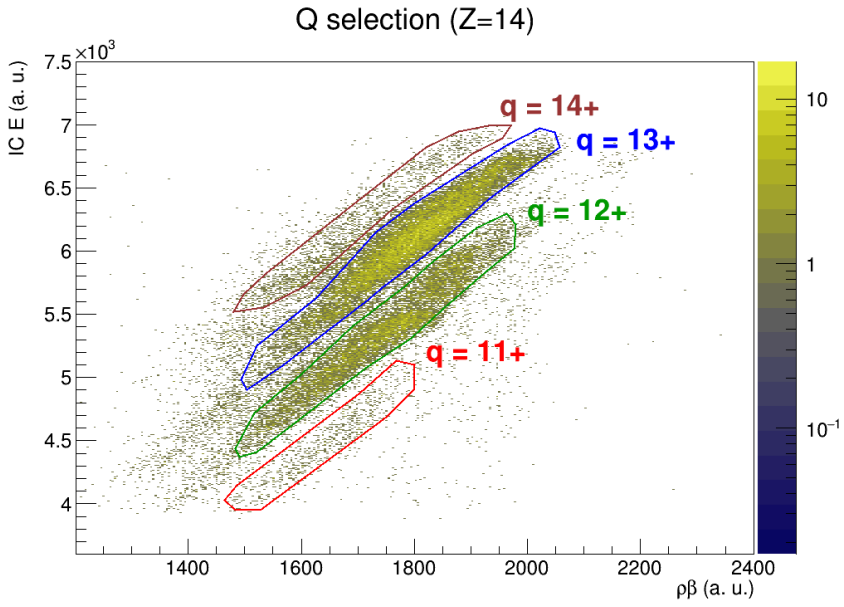

Figure 3.15: E vs $\rho\beta$ matrix from PRISMA relative to $Z = 14$. The displayed cuts allow to select the charge state of the ions.

At this point, the complete identification in A and Z is performed and the γ-ray events can be correlated with a specific reaction channel. From a preliminary analysis, the resolution of the mass identification in PRISMA in this experiment is about $\Delta A/A \sim 1/80$ [35].

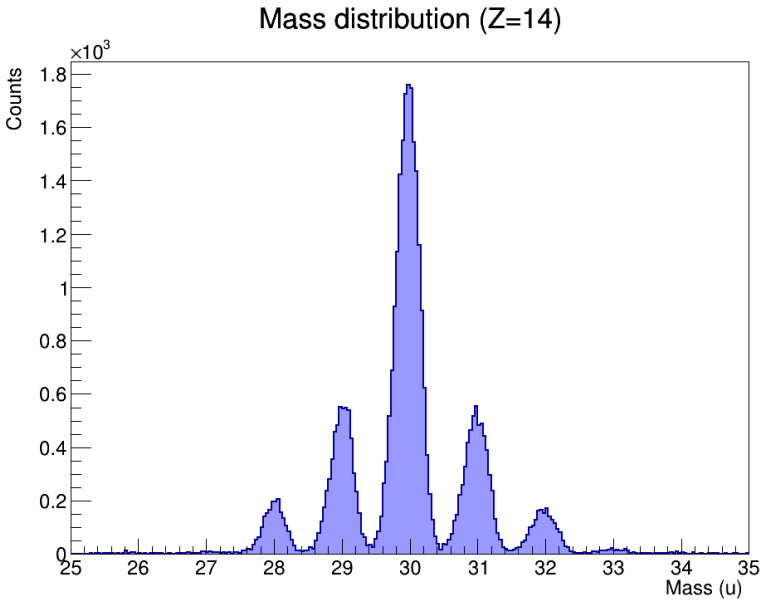

Figure 3.16: Mass number spectrum for $Z = 14$ from the output of the PRISMA data processing.

3.3 PRISMA + AGATA analysis

3.3.1 Coincidence γ rays - ions

After all the steps of the PRISMA presorting, the identification of A and Z is completed for each event and the merging with the AGATA data is possible. The combination of the data is done on the basis of the timestamp and, while in the acquisition phase the trigger was placed on PRISMA alone, and in the replay the *EventMerger* actor sets a window of 2.5 μs, the actual time coincidence window in the analysis is chosen to be much more narrow, in order to avoid contaminations from random coincidences. The window in the analysis is set to be $[-106, -99]$, that can be visualized with the green window in fig. 3.17, corresponding to 7 timestamps (70 ns).

Among the selected events, it is possible to build a γ spectrum in coincidence with a particular transfer channel, thanks to the A and Z identification by PRISMA. This allows to study selectively the γ rays of the two produced nuclei in the binary reaction, which in the case of multi-nucleon transfer can be both in excited states. This means that for each channel, the Doppler correction must be performed separately for the beam-like ion that enters PRISMA, for which the relevant variables are measured directly, and for the heavier binary partner, which needs a kinematical reconstruction. Its reconstruction must take into account the binary reaction process, the energy losses in the target and the emission angle of the beam-like ion, in order to determine the velocity vector of the binary partner for a good Doppler correction.

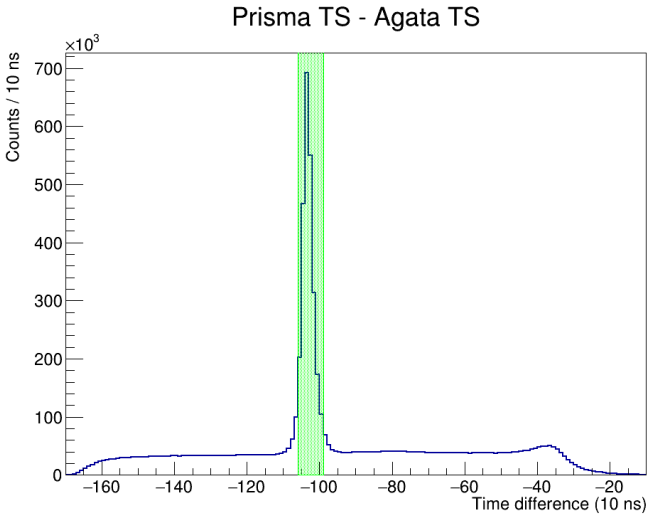

Figure 3.17: Distribution of the difference of timestamp between the AGATA and PRISMA events. The coincidence peak represents the events that show a correlation between a detected ion and γ ray. The green area represents the coincidence gate applied in the processing of the merged data.

3.3.2 Doppler correction

The great advantage of having a complementary detector such as PRISMA is the possibility of measuring the A, Z and velocity of each ejectile. This is a very relevant information in order to perform in-beam γ-ray spectroscopy, because the γ rays that are emitted after the nuclear reaction come from particles moving at relativistic velocities ($\beta \sim 0.09$ in the commissioning experiment). While in the ion rest frame, the γ ray is emitted at the characteristic energy E_0, in the laboratory frame it undergoes a Doppler shift which modifies its energy depending on the velocity of the flying ion β and the angle of the γ emission with respect to the moving direction, θ. In particular, the energy of the photon in the laboratory frame corresponds to

$$E = E_0 \frac{\sqrt{1-\beta^2}}{1-\beta\cos\theta} \tag{3.7}$$

Combining the information of the PSA and tracking of AGATA on the first interaction of the γ in the germanium, with the measured $\vec{\beta}$ of the ejectile ion from PRISMA, the correction for the Doppler shift can be performed on every γ event accurately, by calculating the proper angle θ as the one between the MCP (x, y) detected position and the first γ interaction position in AGATA, combined with the β calculated by PRISMA. After this process, the γ spectrum should show the peaks, which correspond to the γ rays coming from transitions in the flying excited nucleus.

Chapter 4

Performance and optimization

The newest AGATA configuration requires the setup and optimization of different stages of the data processing. In order to have an optimal resolution of the peaks in the gamma-ray spectra, the data processing steps explained in chapter 3 have to be performed. The previous chapter showed the changes in the spectra when modifying the parameters of the processing filters.

In this chapter, the analysis of the final spectra from sources measurement will be presented and evaluated after the optimization of all the steps and the tracking algorithm.

In order to have an additional reference for performances, a simulation of the same experimental setup with radioactive sources has been performed and the performances of real and simulated data are compared in this chapter.

4.1 AGATA simulation software

A simulation package for AGATA and complementary devices is available in order to estimate the performances of the setups when preparing an experiment [37]. The software is based on GEANT4 [38] and allows to obtain simulated γ spectra with a geometry and crystal configuration similar to the one in the experiment. In the case of the presence of particle detectors, the simulation allows to obtain directly the Doppler corrected spectra with the same condition as the in-beam experiment.

In this work, the software was used to simulate the detection of γ rays from the same radioactive sources that were used before the experiment for the calibrations and the evaluation of the performance. In particular, sources of ^{60}Co, ^{133}Ba and ^{152}Eu have been simulated. The configuration of the active ATCs and target chamber has been included to match the experimental conditions. The simulation of each source involved $2 \cdot 10^6$ events. The simulation of the γ rays creates first a file containing the interactions of the photons in the crystals, and then the OFT tracking code must be applied. The calculations on the simulated spectra that will be presented are already considering the optimized tracking parameter, that will be studied in section 4.3.

Figure 4.1 shows the comparison between the simulated and measured tracked spectra, normalized by the number of decaying nuclei. The main difference between simulations and real data is the distribution of the background. In the simulation, the only background comes from the Compton continuum of the observed peaks, while in the measurements there are other sources of background such as cosmic rays, environmental radiation and, since these measurements were taken at the end of the commissioning experiment, materials activated by the beam irradiation. Evidence of this latter behaviour is the presence of an annihilation peak at 511 keV visible in the measured spectra of ^{60}Co and ^{152}Eu and absent in the simulations. The level of the background in the real data is especially higher at energies lower than $\sim$ 500 keV. As it is visible, the experimental spectra include a cut for low energy that does not allow to see any significant data below $\sim$ 50 keV, while the simulation does not have this feature and some peaks are visible also below this threshold, as in fig. 4.1a. Furthermore, simulated spectra show a higher photo-peak efficiency since the height of the γ-ray peaks is larger.

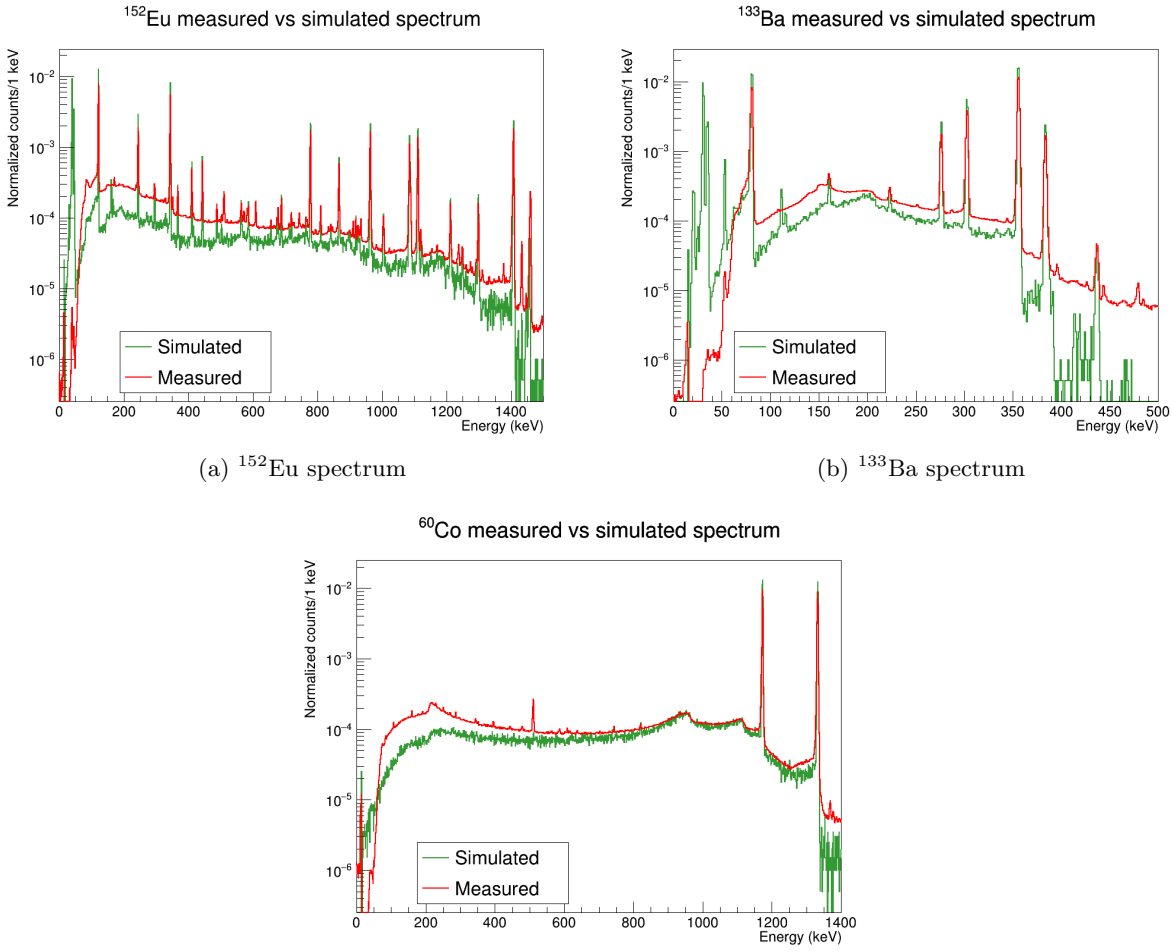

(a) ^{152}Eu spectrum

(b) ^{133}Ba spectrum

(c) ^{60}Co spectrum

Figure 4.1: Comparison of measured and simulated tracked spectra for the sources that are used in the analysis. The measured spectra are normalized to the calculated number of decaying nuclei from the activity of the sources, while the simulated ones are normalized to the number of simulated events.

4.2 γ-γ coincidence

The timing information of the γ interactions allows to select correlated events that are emitted in coincidence by the source or in the experiment. The main purpose of this correlation is to observe the γ-ray cascades that are emitted by an excited nucleus. The fast emission of two consecutive γ-rays results in a time correlation between the events, if they are both detected by AGATA.

In the *EventBuilder*, a first wide coincidence window is applied to the events with hit multiplicity larger than one. In the later analysis, however, a more restrictive condition is applied to build the γ-γ matrices, the 2D spectra populated by the energies of two γ rays detected in coincidence. Figure 4.2 shows the time difference spectra (in absolute value) of the detected γ in an event with the applied cuts on the timing to build the γ-γ coincidence. Plot 4.2a shows the difference of timestamp from the core signals detected inside one event. The applied cut is for a time difference of less than 10 timestamps, equal to 0.1 μs. Plot 4.2b instead shows the difference of time of tracks belonging to the same event. The resolution of the time of the tracks is higher than the core timings, because there is an additional CFD filter that calculates more precisely the time of the first interaction of the photon. Also in this case, the coincidence window is 10 timestamps.

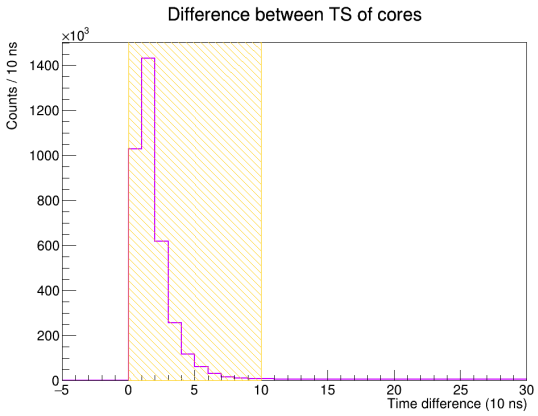

(a) Absolute value of time difference distribution between two core signals in one event. The yellow area represents the 10 timestamps coincidence window.

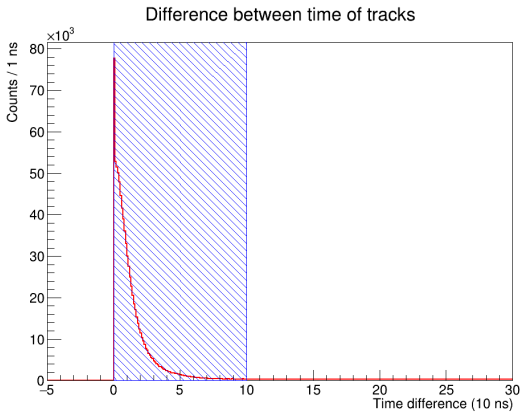

(b) Absolute value of time difference distribution between two reconstructed tracks in one event. The blue area represents the 10 timestamps coincidence window.

Figure 4.2: Time difference distributions for core signals and tracks inside one event. The coloured areas represent the coincidence window applied in the γ-γ correlation.

After the coincidence window, the γ-γ matrices are obtained. An example is shown in fig. 4.3, where the matrices are shown for the core and tracked signals with a ^{60}Co run. The lines related to the peaks at 1173 keV and 1332 keV are strongly populated, but especially the intersections between the two peaks are especially intense, showing that the two transitions are correlated in the decay.

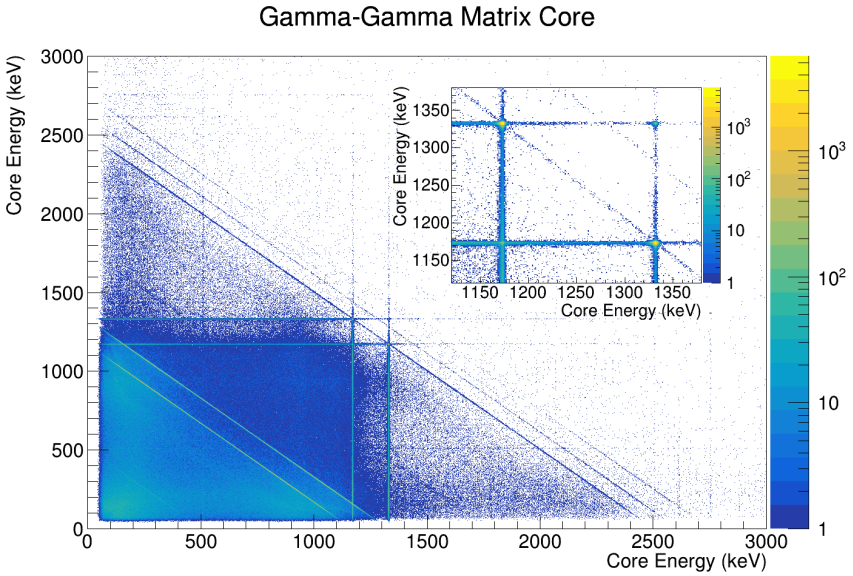

(a) γ-γ matrix for core energies produced with a 10 ns coincidence window. The inset shows a zoom on the energies of the two peaks of ^{60}Co.

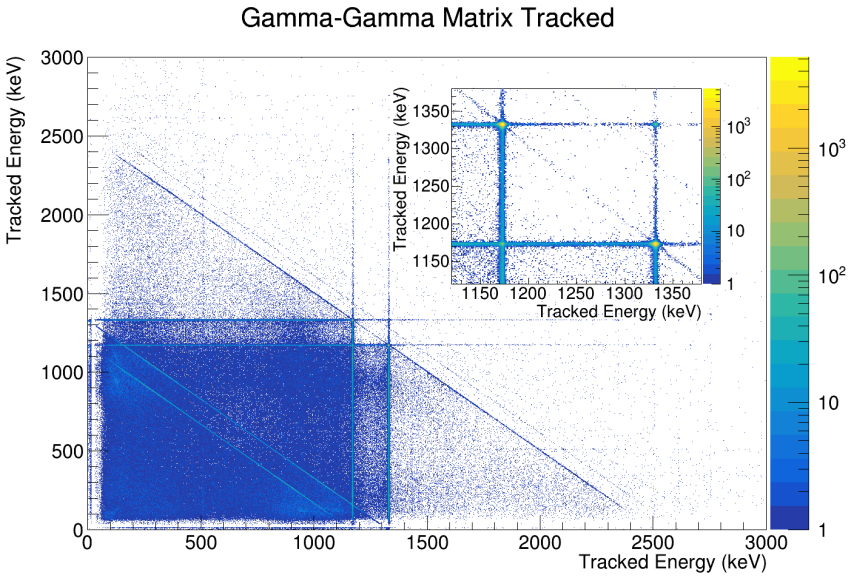

(b) γ-γ matrix for tracked energies produced with a 10 ns coincidence window. The inset shows a zoom on the energies of the two peaks of ^{60}Co.

Figure 4.3: γ-γ matrices for core and tracked energies coming from a measurement of a ^{60}Co source.

In the tracked matrix (fig. 4.3b), the intersection of the two ^{60}Co peaks is even more intense, while the contaminant coincidences that populate the other regions of the matrix are reduced. In particular, the events belonging to the triangular structure close to the origin of fig. 4.3a are significantly cut after the tracking. This happens because the partial energy deposits contribute to the reconstruction of the full-energy γ rays. The two diagonal lines close to the bottom left corner correspond to two different entries in the matrix that sum up to the total energy of one of the two γ rays of ^{60}Co. The fact that the lines are visible also in the tracked matrix, means that

the tracking algorithm has a certain accuracy, but there are still events that are not recognized as a single track correctly and therefore they populate these linear structures. This can happen especially if there is a back-scattering of a photon, where the two successive interactions might be on opposite sides of AGATA and the tracking algorithm struggles with the clustering of the two hits with a large angular separation. A similar behaviour happens also with the diagonals at ∼2500 keV, where similar structures appear due to the sum peaks of 1173 keV and 1332 keV.

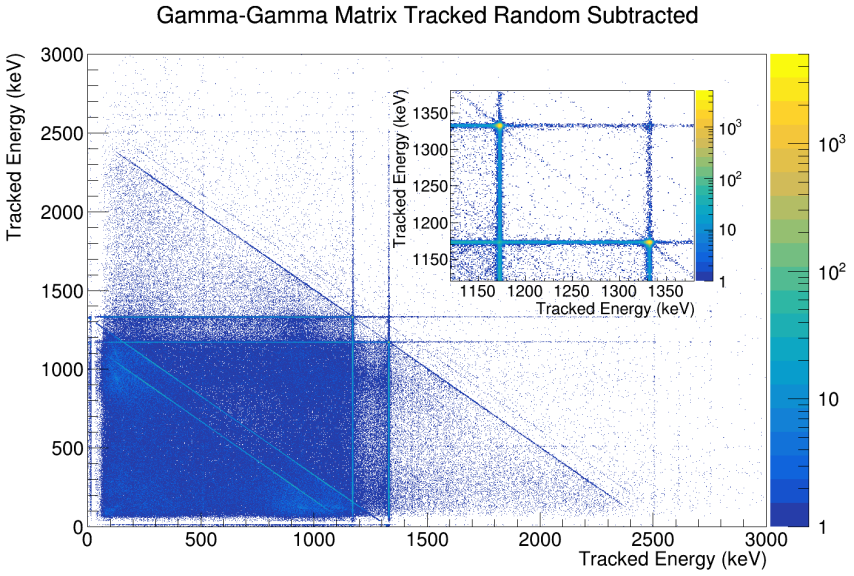

(a) γ-γ matrix for tracked energies after the subtraction of the events due to random coincidences. The inset shows a zoom on the energies of the two peaks of ^{60}Co.

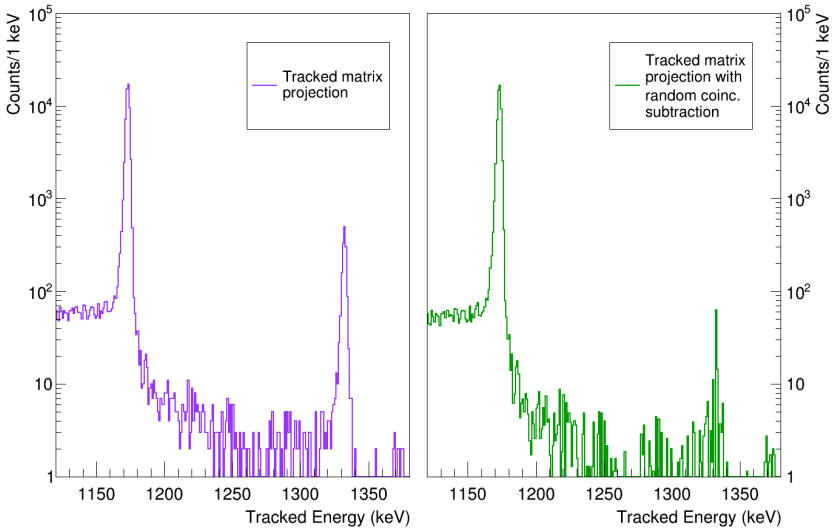

(b) Projection of the γ-γ matrix on the interval (1325,1338) keV before (left) and after (right) the subtraction of random coincidences.

Figure 4.4: γ-γ matrix with tracked energies after the subtraction of random coincidences and comparison of the projections of the matrix before and after the random coincidence subtraction.

Although the time condition on the γ-γ coincidence was restricted to the peak close to a time difference of 0 and a large fraction of the events belong to the 1.1 MeV-1.3 MeV cascade in ^{60}Co, it is possible to see a concentration of counts of self-coincidence for the two transitions in the matrices in the insets of figs. 4.3a-4.3b. This is due to the fact that in the time window there are random coincidences, given by two similar γ emissions happening simultaneously and the two photons being detected at the same time in AGATA. In order to get rid of these uncorrelated events, the following procedure was performed. Another γ-γ matrix with tracked γ rays was built by putting a gate on the time difference far from the coincidence peak, in the range [150,500] ns. The obtained matrix of random coincidence events was rescaled by the ratio of the two gating intervals and subtracted from the tracked γ-γ matrix. The result is the matrix in fig. 4.4a, where the self-coincidence peaks have almost disappeared. To see better the effect of this operation, fig. 4.4b shows the projection of the two tracked γ-γ matrices (before and after random coincidence subtraction) in the range [1325,1338] keV, *i.e.* with a gate on the higher-energy peak of ^{60}Co. With an ideal coincidence, only the other peak at 1173 keV would be visible, but in the left plot, before the subtraction, a small peak of self-coincidence at 1332 keV is visible. However, after the subtraction of the random coincidences, the self-coincidence peak has effectively disappeared, as in the right plot. By estimating the ratio of the integral of the self-coincidence peak with respect to the 1.1 MeV peak in the two cases, the value before the subtraction was 2.64(14)%, while after the subtraction it reached 0.16(2)%, therefore almost all self-coincidence was suppressed.

4.3 Tracking Optimization

The basics of the tracking algorithm were presented in section 2.2.5. With each experiment, it is possible to tune the parameters in the OFT algorithm to maximize the absolute efficiency or the peak-to-total ratio in a region of interest in the γ spectra. The tuning of the parameters also affects the width of the peaks, which is another estimator to control.

In the commissioning experiment, the objective is to look at γ spectra of different isotopes, which have peaks that range from around 100 keV to over 4 MeV, so there is not one single peak for which to optimize the parameters of the tracking algorithm. The choice in this section was to refer to the 1.3 MeV peak of the ^{60}Co source and to study the dependence of three estimators on different values of the OFT parameters. The optimal parameters were then selected as those that maximize the counts in the area of the 1.3 MeV peak, which is equivalent to maximizing the absolute photopeak efficiency. In this analysis, the peaks were fitted with simple Gaussian curves, therefore additional shape corrections were not accounted for and the widths may result larger than in the rest of the thesis, where more realistic functions were used to fit the peaks.

The three tunable parameters are the σ_θ, $min_{P_{track}}$ and $ClAngRed$, which have been defined in section 2.2.5. The OFT algorithm was run on the same input file of PSA hits, generated in a replay of a ^{60}Co source measurement. The σ_θ, $min_{P_{track}}$ and $ClAngRed$ parameters were varied respectively in the intervals $[0.5, 1.5]$, $[0, 1]$ and $[1, 4]$, following a similar analysis performed in

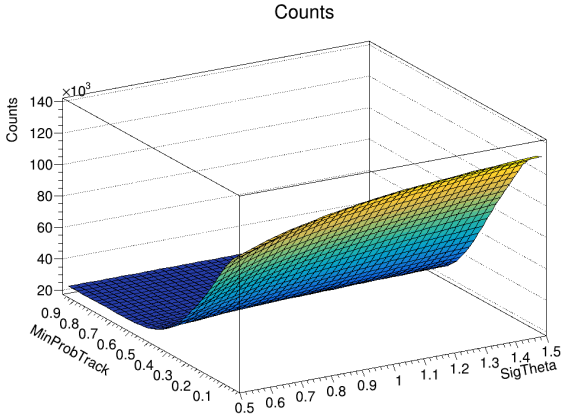

(a) Background-subtracted counts in the 1.3 MeV peak.

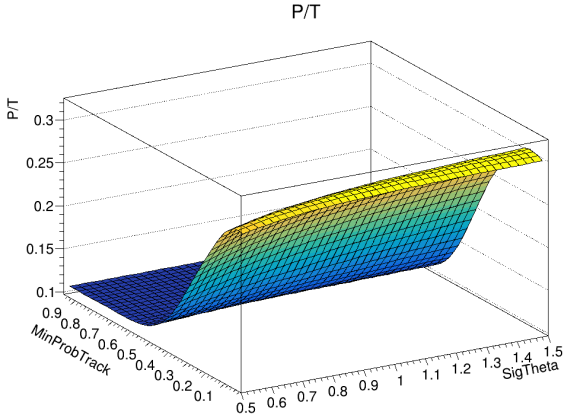

(b) Peak-to-total ratio.

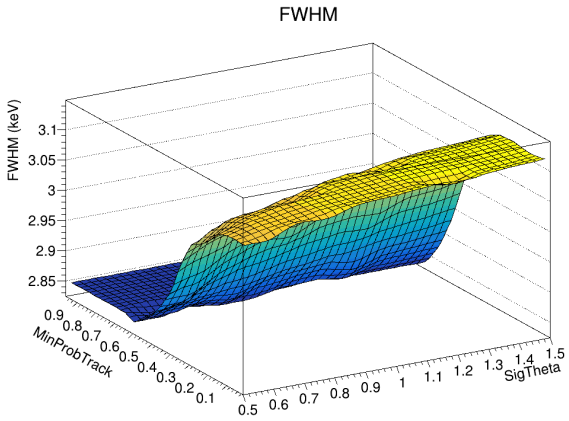

(c) FWHM of the 1.3 MeV peak.

Figure 4.5: Dependence of the three estimators on different values of σ_θ and $min_{P_{track}}$. In these plots, $ClAngRed$ was fixed to 3.

ref. [39]. The estimators that were examined were the background-subtracted counts in the 1.3 MeV peak in the singles spectrum, the peak-to-total ratio and the FWHM of the 1.3 MeV peak. In this analysis, the peak-to-total ratio (P/T) is defined as

$$P/T = \frac{\text{sum of bg} - \text{subtracted integrals of the two peaks of } {}^{60}Co}{\text{Integral of spectrum in } [0, 1400]\,\text{keV}} \tag{4.1}$$

A first coarse grid search was performed in the whole ranges of the three parameters and then a finer one was used to optimize the value of the single parameters. Figure 4.5 shows the variation of the counts, P/T and FWHM over the complete ranges of σ_θ and $min_{P_{track}}$. The efficiency and peak-to-total seem to be maximized when the value of $min_{P_{track}}$ is small, and increases slightly with σ_θ. The width of the peak increases simultaneously with the counts. Since the aim was to optimize the efficiency alone, the values of the parameters that achieved this were $\sigma_\theta = 1.5$ and $min_{P_{track}} = 0.01$. Then, fixing these two parameters, the $ClAngRed$ parameter was varied and the estimators were again calculated for each combination, as seen in fig. 4.6. In this range, the

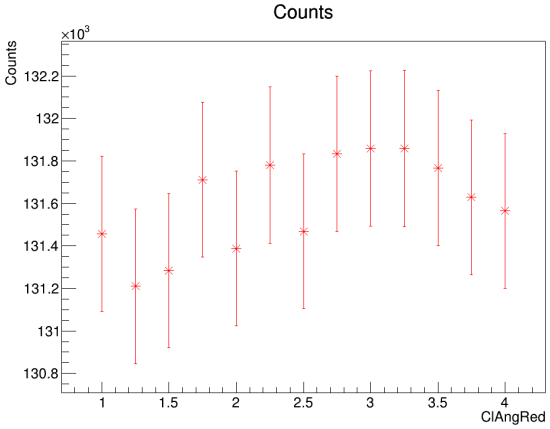

(a) Background-subtracted counts in the 1.3 MeV peak.

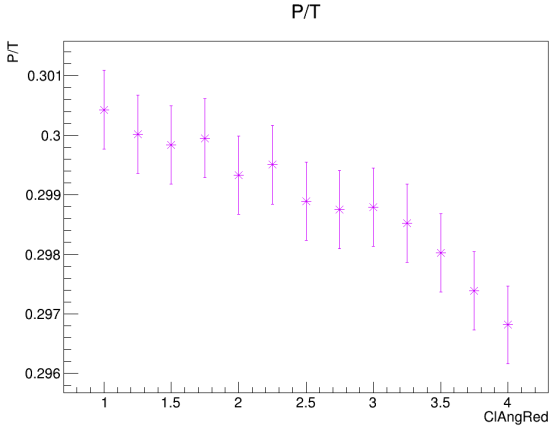

(b) Peak-to-total ratio.

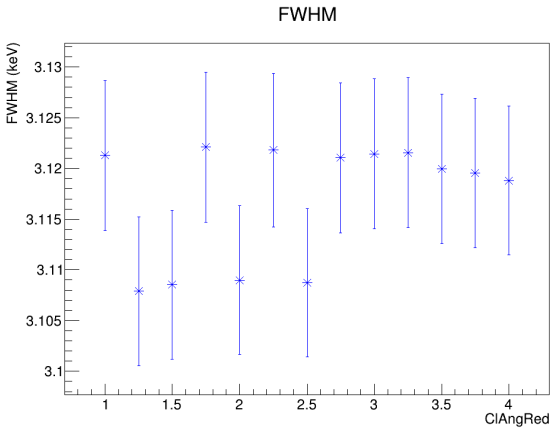

(c) FWHM of the 1.3 MeV peak.

Figure 4.6: Dependence of the three estimators on the $ClAngRed$ parameter. In these plots, σ_θ was fixed to 1.5 and $min_{P_{track}}$ to 0.01.

value that maximized the counts was $ClAngRed = 3$, so it was chosen as the optimal value.

Therefore $\sigma_\theta = 1.5$, $min_{P_{track}} = 0.01$ and $ClAngRed = 3$ were the tracking parameters that were selected in the analysis.

The improvement in efficiency of this set of parameters can be understood from fig. 4.7, where the same ^{60}Co spectrum is shown after the tracking algorithm with two different sets of parameters. The red histogram was obtained with the optimized parameters for the efficiency of the 1.3 MeV peak, while for the green histogram, the default set of parameters was used: $\sigma_\theta = 0.8$, $min_{P_{track}} = 0.05$ and $ClAngRed = 1$ [40]. The plot shows two regions of the spectrum. On the left, the low-energy Compton background region is displayed (with a contamination peak at 511 keV), while on the right a detail of the 1.3 MeV peak of ^{60}Co is shown. The optimized spectrum shows a higher number of counts in both of the regions, which means a larger efficiency. Moreover, the integral of the optimized spectrum in the displayed Compton region is larger by 4% with respect to the non-optimized tracking, and for the peak at 1.3 MeV the increase

in the integral reaches 6% with respect to the default parameters. Therefore, with this set of parameter, a higher absolute efficiency is obtained for the peak, even though there is also an increase in the background counts.

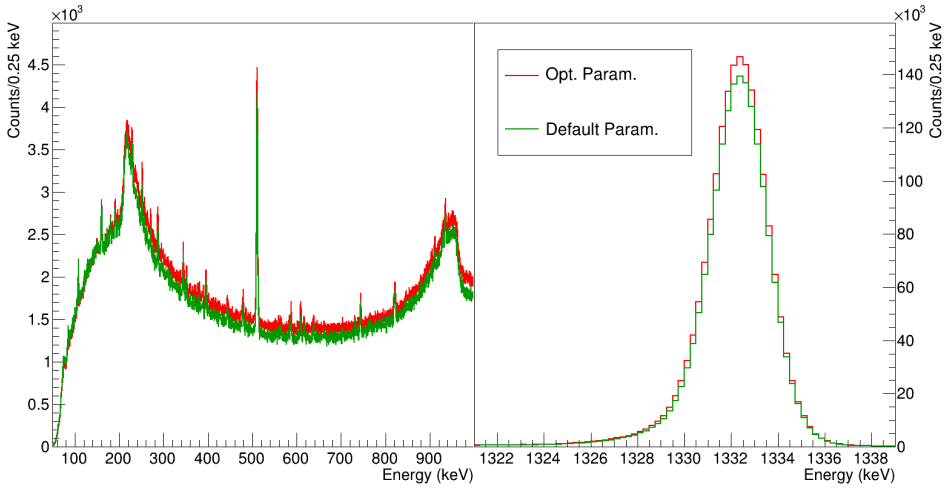

Figure 4.7: Comparison of a ^{60}Co tracked spectrum with two sets of parameters for the OFT algorithm. The red histogram was obtained with the optimized for the efficiency of the 1.3 MeV peak, while the green histogram was obtained with the default set of OFT parameters.

4.4 Energy Resolution

The width of the γ peaks is an important parameter in the performances of AGATA. Having sharp peaks, *i.e.* a better resolution, is important to discriminate more efficiently peaks that are close together.

The steps in the data processing of AGATA are optimized to correct for the effects that worsen the resolution, such as cross-talk between segments and the partial charge collection due to neutron damage to the germanium, as well as to calibrate the local energy spectra of the crystals, in order to obtain a global spectrum with sharper peaks.

The FWHM of the peaks of the radioactive sources as a function of the energy of the peak are reported in fig. 4.8, for the core and the tracked spectra. The peaks were fitted with the standard peak shape from RadWare [41] and the measured FWHM are in the range 2.0−3.0 keV, with the widths that on average increase with the energy. It is also visible how the tracking reconstruction affects more the γ rays at higher, since the discrepancy of FWHM between core and tracked spectrum is larger at energies higher than $\sim$ 700 keV.

Normalizing the FWHM by the energy of the centroid of the peak, the energy resolution is defined:

$$R(E_\gamma) = \frac{FWHM(E_\gamma)}{E_\gamma} \tag{4.2}$$

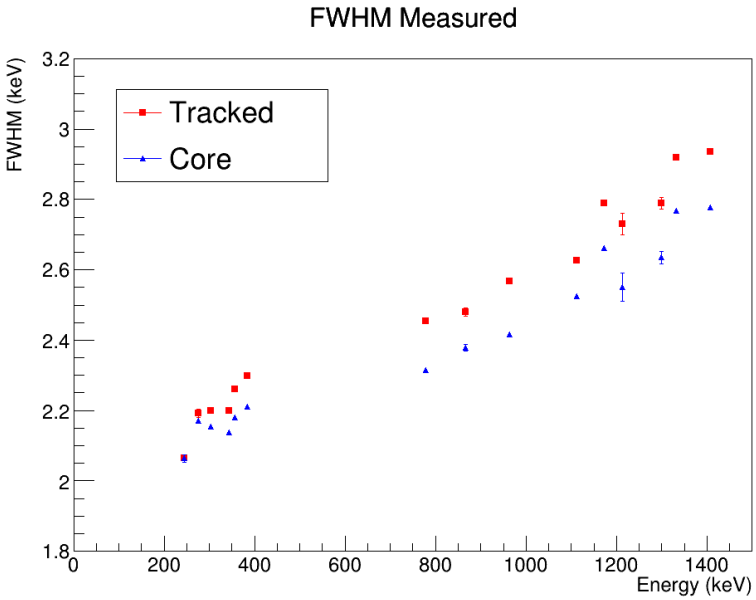

Figure 4.8: FWHM as a function of the peak energy. The values are measured from the peaks in the sources spectra.

The plot of the energy resolution as a function of the energy of the peak is shown in fig. 4.9. The range of resolution is between 2‰ and 9‰ and it reaches the higher values only at energies below 500 keV, while for higher energies, the resolution settles around 2-3‰.

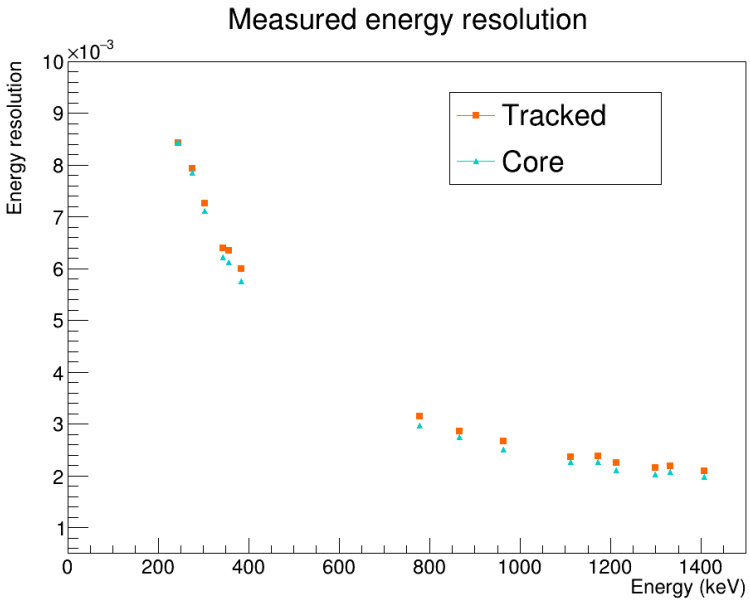

Figure 4.9: Resolution as a function of the peak energy. The values are measured from the peaks in the sources spectra.

4.5 Efficiency and Peak-to-total

4.5.1 Definitions

The interaction of γ rays in matter is a stochastic process, which probability depends on the medium and the photon energy. Consequently, not all the γ rays that pass through the germanium crystals will release their energy and be detected. Therefore, with a γ-ray spectrometer such as AGATA, the evaluation of the detection efficiency is an important task to have a reference value in experimental measurements. This test is done using static radioactive γ-ray sources.

Different definitions of efficiency can be given. The *absolute efficiency* is defined as :

$$\epsilon_{abs} = \frac{\text{number of detected } \gamma}{\text{number of } \gamma \text{ emitted by the source}} \tag{4.3}$$

while the *intrinsic efficiency* of the detector can be defined as:

$$\epsilon_{int} = \frac{\text{number of detected } \gamma}{\text{number of } \gamma \text{ incident on the detector}} \tag{4.4}$$

The *geometric efficiency*, instead, is defined as

$$\epsilon_{geom} = \frac{\Omega}{4\pi} \tag{4.5}$$

where Ω represents the fraction of the full solid angle which is subtended by the detector from the source position. These three quantities are related via the relation:

$$\epsilon_{abs} = \epsilon_{int} \cdot \epsilon_{geom} \tag{4.6}$$

For the interest of γ-ray spectroscopy, more than the efficiency of interaction with the detector, the relevant quantity refers to the counts that appear in the photo-peak. Therefore, in this section the calculations will refer to the *absolute photo-peak efficiency*:

$$\epsilon_{photo} = \frac{\text{number of counts in the photo} - \text{peak}}{\text{number of } \gamma \text{ emitted by the source}} \tag{4.7}$$

Other than the detection efficiency, another parameter which is important to calculate is the peak-to-total ratio, defined as:

$$P/T = \frac{\epsilon_{photo}}{\epsilon_{total}} = \frac{\text{number of counts in the photo} - \text{peak}}{\text{Total counts in the spectrum}} \tag{4.8}$$

This represents the fraction of the total interactions in the detectors that release the full energy of the γ ray, quantifying the number of photo-peak events with respect to the total hits.

4.5.2 Methods

To evaluate the efficiency, radioactive γ-ray sources were placed at the center of the reaction chamber. Since the commissioning experiment was performed at the nominal position of AGATA, the efficiency measurements were done in the same configuration, for which the center of the chamber corresponds to the center of AGATA. This meant an average distance of 23.5 cm between the source position and the edge of the ATCs. In this section, the analysis methods for calculating the efficiency will be presented. For further details on the formulas and calculations, ref. [21] can be consulted.

By comparing the detected counts in the spectrum and the expected counts emitted by the source the absolute photo-peak efficiency can be computed:

$$\epsilon_{photo}(E) = \frac{N_\gamma(E)}{(1 - D_t) \cdot A \cdot I_R(E) \cdot \Delta t} \tag{4.9}$$

where $N_\gamma(E)$ is the number of counts in the peak with energy E, D_t is the dead time of the acquisition system, A is the activity of the source, $I_R(E)$ the relative intensity of the γ transition with energy E and Δt is the time interval of the measurement. From the energy spectrum, the number of counts is extracted from the total area under the peak after background subtraction.

The absolute efficiency was also calculated for the simulated data, where D_t was set to 0 and the quantity $A \cdot \Delta t$ was substituted with the number of simulated decaying nuclei.

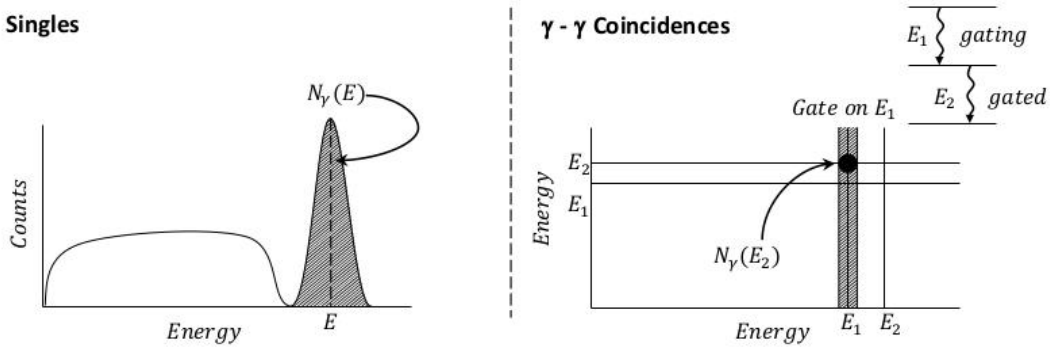

Figure 4.10: Scheme of the two methods for the calculation of the absolute photo-peak efficiency. Taken from ref. [21]

This is the method for the calculation of the efficiency *in singles*, which is represented on the left plot of fig. 4.10. There is, however, another method to calculate the efficiency and it exploits known γ cascades in the decay of the sources that are used. It is called efficiency *in coincidences* (right plot of fig. 4.10) and consists in setting a gate on the events where the upper transition (energy E_1) in the cascade has been detected and measure the counts of the lower transition (energy E_2) that are in time coincidence with the first one, normalizing them to the counts of the upper transition in singles. Using this technique to get the efficiency allows to get rid of dependencies from the dead time and the source activity.

Referring to the right plot of fig. 4.10 for the names of the transitions, the full expression for the efficiency of the transition at energy E_2 is calculated as:

$$\epsilon_{photo}(E_2) = \frac{N_{\gamma,coinc}(E_2)}{N_{\gamma,sing}(E_1) \cdot W(\theta) \cdot 1/(1+\alpha_T(E_2))} \tag{4.10}$$

where $N_{\gamma,coinc}(E_2)$ are the counts in the peak at E_2 in the gated spectrum, $N_{\gamma,sing}(E_1)$ are the counts in the peak at E_1 in the singles spectrum, $W(\theta)$ is the angular correlation function of the two successive γ rays and $\alpha_T(E_2)$ is the internal conversion coefficient from the state at energy E_2. While the efficiency in singles can in principle be measured for all the γ rays emitted by a source, the coincidence analysis is possible only with successive transitions. In this analysis, the sources which have been used are ^{60}Co, ^{133}Ba and ^{152}Eu, so the coincidence analysis was performed only with the transitions listed in table 4.1, where the energies of the γ rays, the angular momenta of the involved states and the internal conversion coefficients for the intermediate states are reported. The angular correlation function in eq. 4.10 is defined as:

$$W(\theta) = \sum_{k=0,2\ldots} A_k(j_1\lambda_1 j\lambda_2 j_2) P_k(\cos\theta) \tag{4.11}$$

The order k_{max} is given by $k_{max} = min\{2\lambda_1, 2\lambda_2, 2j\}$. P_k is the Legendre polynomials of order k. The coefficients A_k are dependent on the angular momentum of the involved states and the multipolarity of the transition. Their value in the relevant cases is reported in table 4.2.

Table 4.1: Information relative to the γ-ray cascades in the used radioactive sources. Conversion coefficients taken from [42]

Source	Daughter	$j_1 \to j \to j_2$	E_1	E_2	$\alpha_T(E_2)$
^{60}Co	^{60}Ni	$4 \to 2 \to 0$	1173.2	1332.5	0.0001625(23)
^{152}Eu	^{152}Gd	$3 \to 2 \to 0$	778.9	344.3	0.0398(6)

Table 4.2: Coefficients of the angular correlation function relative to the γ-ray cascades in the used radioactive sources. Taken from [43]

Nucleus	$j_1 \to j \to j_2$	λ_1	λ_2	A_2	A_4
^{60}Ni	$4 \to 2 \to 0$	E2	E2	0.1020	0.0091
^{152}Gd	$3 \to 2 \to 0$	E1	E2	-0.0714	0

The peak-to-total ratio is computed in the same way as defined in eq. 4.1. The result will be shown for ^{60}Co as a reference.

4.5.3 Results

Absolute photo-peak efficiency is measured for different peaks of the sources and the values are plotted as a function of energy. They are fitted with the RadWare function [41]:

$$\epsilon_{photo}(E_\gamma) = exp\left[[(A + Bx + Cx^2)^{-G} + (D + Ey + Fy^2)^{-G}]^{-1/G}\right] \tag{4.12}$$

$$\text{with} \qquad x = \ln\frac{E_\gamma}{100\,\text{keV}} \qquad y = \ln\frac{E_\gamma}{1\,\text{MeV}}$$

The parameter C is fixed to 0, as described in ref. [44], and G is fixed to 15 since similar values are usually set [21, 44], while the other ones are fitted to the points. To perform the fit, the absolute values of efficiency have been multiplied by a factor 100, therefore the curves are already in the units of % as it is displayed in the following plots.

For the fit of the efficiency curve, peaks from the three sources were used, but there might be some discrepancy between them coming from the estimation of the dead time. The ^{152}Eu source, in fact, had a significantly lower activity that caused negligible dead time, while for the other two sources, the acquisition were affected by dead time that was estimated from an average on the measurement time. Therefore, the value assumed for the dead time of ^{60}Co and ^{133}Ba was a rough estimate.

The absolute efficiency curve for measured and simulated γ rays are shown, respectively, in figs. 4.11a-4.11b. The parameters of the fitted efficiency curves are reported in table 4.3. The tracked measured efficiency curve fails to fit appropriately the low energy part of the function 4.12, as seen from the parameters A and B, compatible with 0. The parameters obtained from the fit of the simulated curves are not reliable, since the uncertainty on the points is really small.

Table 4.3: Parameters of the fitted efficiency curves.

Method	A	B	D	E	F
Core Meas.	2.18(6)	-0.50(4)	1.2(3)	-0.7(6)	-0.16(12)
Tracked Meas.	5(4)	0.1(10)	1.268(9)	-0.42(2)	-0.063(10)
Core Sim.	2.182(3)	-0.21(6)	1.0854(4)	-0.4598(14)	0.0312(18)
Tracked Sim.	2.0970(14)	-0.118(3)	1.4566(4)	-0.4106(16)	0.017(3)

Figure 4.12 shows the comparison of the simulated and the measured efficiency values in both the tracked and the core spectra. The simulated values are above the measured in both cases, but the discrepancy in the case of the core efficiency ($\sim$ 3.5% more) is less important than in the case of tracked γ rays ($\sim$ 17% more). This is due to the fact that the tracking algorithm on the simulated data is much more efficient, given the fact that the interaction positions are not obtained through the PSA but they are given directly from the simulation.

In fig. 4.13, the points for the efficiency in coincidence are shown together with the measurements obtained with the spectra in singles. The coincidence measurements are obtained for both the core and tracked spectra. As for the efficiency in coincidence of the tracked spectrum (dark green), there is an effect to correct. During the tracking algorithm, interactions in coincidence within a certain solid angle are clustered together, therefore two photons in a cascade which

are emitted with a small angular separations will be likely not recognized separately by the algorithm. This means that the tracked spectra are missing a fraction of the events in the coincidence efficiency measurement. This behaviour can be seen in fig. 4.14, where in the example of the 778 keV - 344 keV cascade in ^{152}Gd (^{152}Eu source), the normalized distribution of the relative angle (bottom plot) drops to 0 for small angles. This means that for small separation angles, the counts in the coincidence tracked spectrum are lower than the real ones. To correct this effect, on the normalized angular distribution the theoretical angular correlation function $W(\theta)$ was fitted as in eq. 4.11 with the corresponding A_k parameters reported in table 4.2 and with a free normalization coefficient. In the example of ^{152}Gd, the process can be seen in fig. 4.15a. The theoretical function, which describes the distribution at every possible θ, is used to multiply the angular distribution of uncorrelated tracked γ rays, as the middle histogram of fig. 4.14, which does not include the loss at small angles given by correlated γ rays. Thanks to this operation, a corrected angular distribution for the correlated photons in the cascade is obtained and it is compared to the measured one as in fig. 4.15b. This corrected distribution covers also the small angles and the counts in this histogram are added up to compute the corrected value of the coincidence efficiency for the tracked γ rays.

The points in fig. 4.13 show the effect of the correction. The coincidence efficiency for the core (light green) for the 778 keV - 344 keV cascade falls above the fitted efficiency curve, but still compatible within the uncertainty of the measured point. For the cascade in ^{60}Ni, the value is instead slightly lower than the curve. The tracked coincidence after the correction for small angles shows a value for the 778 keV - 344 keV cascade that is well aligned with the tracked absolute efficiency curve, while the point at 1332 keV is a little higher than the curve.

The agreement of the coincidence efficiency with the measured absolute efficiency values at the same energy is not perfect and the reason might be an inaccurate subtraction of the background for the coincident counts. Further analysis will be done to explain and correct the efficiency values that were observed.

The peak-to-total ratio was calculated using eq.4.1 on the core and tracked spectra of the ^{60}Co source. The integral of the 511 keV contaminant peak from activated material was subtracted from the normalization counts. The reference values for absolute efficiency at 1.3 MeV for ^{60}Co and peak-to-total ratio are shown in table 4.4 for measured and simulated data.

Table 4.4: Absolute efficiency and peak-to-total (P/T) calculated for measured and simulated ^{60}Co spectra

Spectrum type	Efficiency (%)	P/T (%)
Measured Core	2.52(7)	17.383(12)
Measured Tracked	3.24(9)	30.328(19)
Simulated Core	2.604(2)	21.17(8)
Simulated Tracked	3.785(4)	44.10(14)

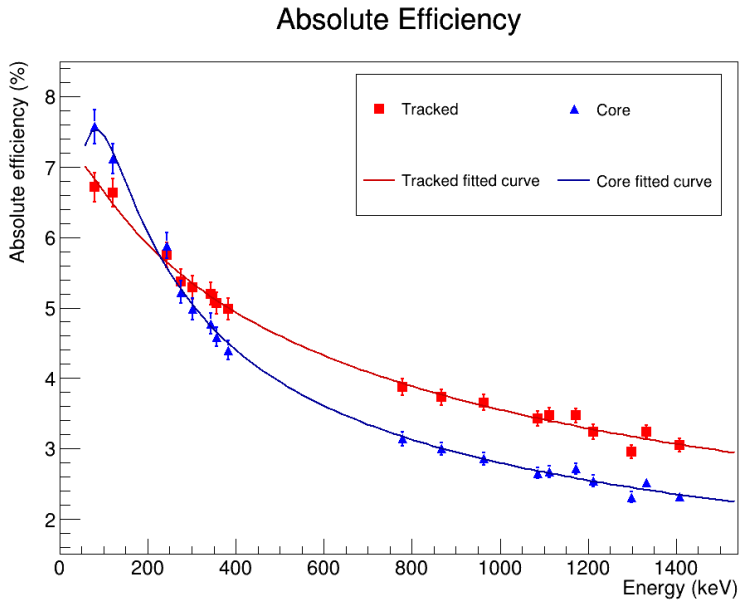

(a) Absolute photo-peak efficiency curve from sources measurements.

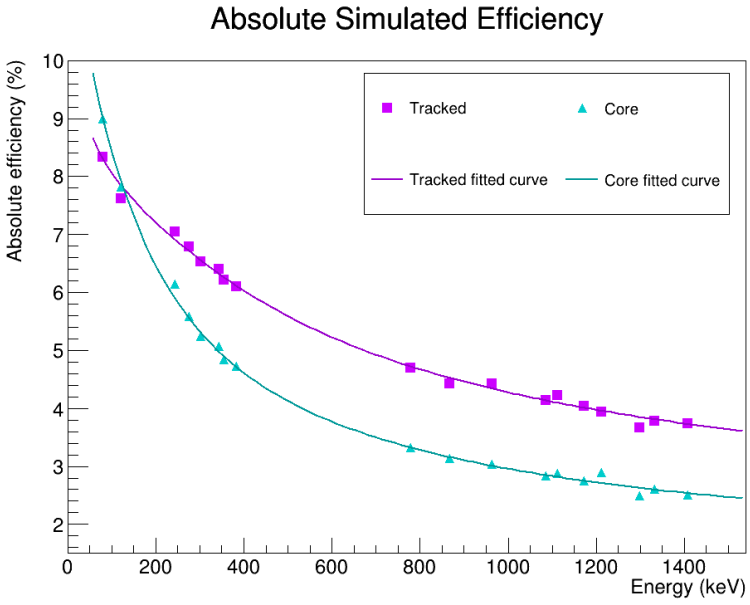

(b) Absolute photo-peak efficiency curve from sources simulations.

Figure 4.11: Measured and simulated fitted efficiency curves obtained from core and tracked γ spectra.

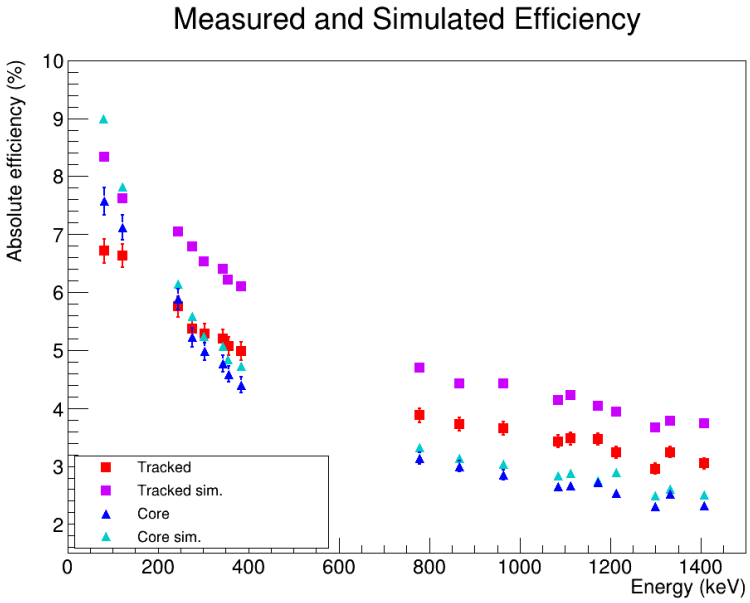

Figure 4.12: Comparison of measured and simulated efficiency obtained from core and tracked γ spectra.

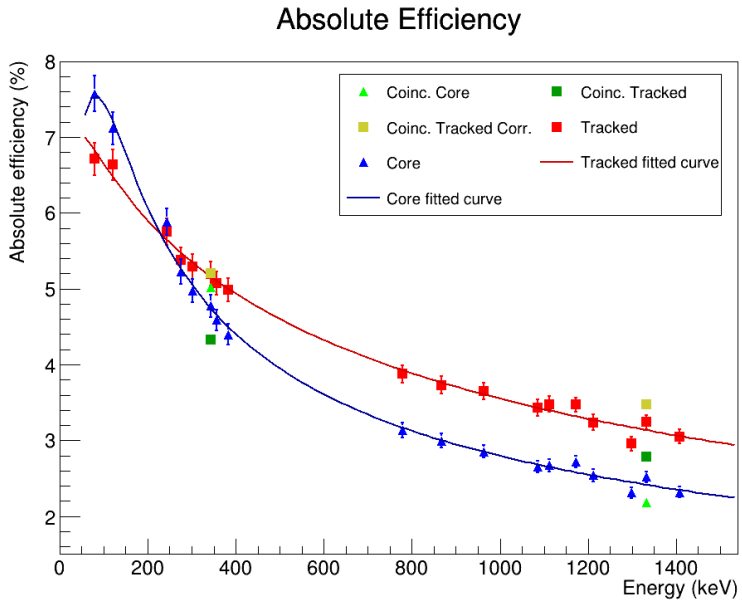

Figure 4.13: Measured efficiency obtained from core and tracked γ spectra and coincidence efficiency for the considered γ-ray cascades.

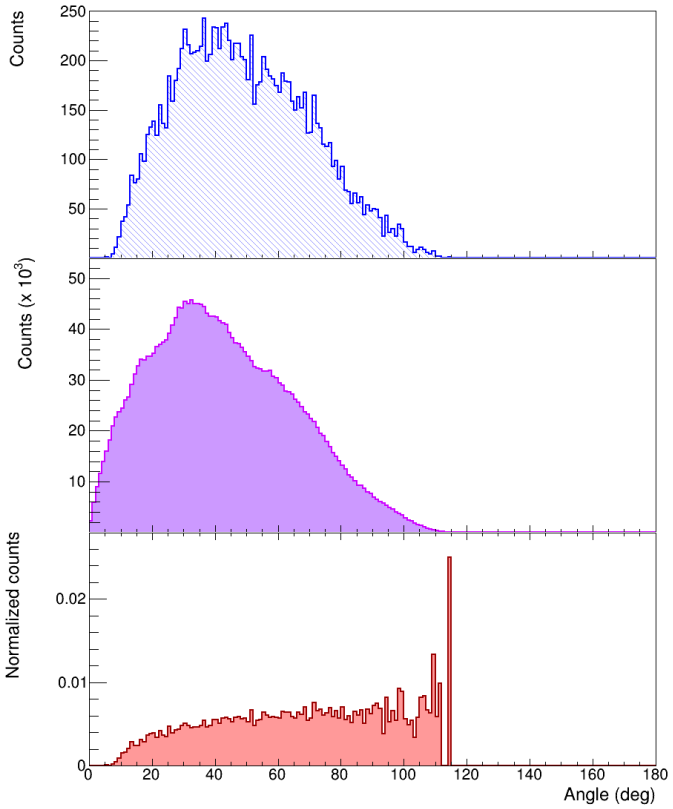

Figure 4.14: Angular distributions for tracked γ rays in the ^{152}Gd 778 keV - 344 keV cascade. The top plot represents the background-subtracted angular separation distribution of the γ rays in coincidence. The middle plot shows the angular separation distribution of two uncorrelated γ rays in the same energy ranges. The bottom plot is the normalized angular distribution: it corresponds to the histogram on the top plot normalized to the histogram in the middle plot.

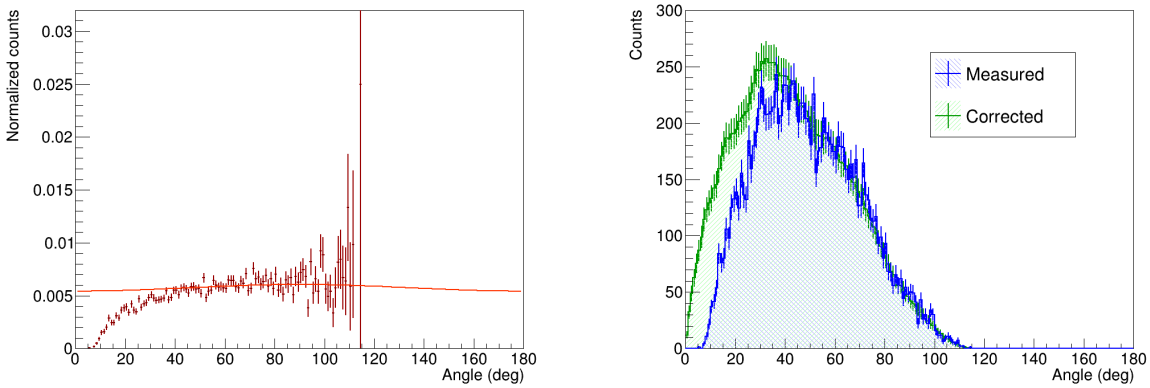

(a) Normalized angular distribution (same as bottom of fig. 4.14) with theoretical curve for 344 keV - 778 keV cascade in ^{152}Gd fitted in red.

(b) Measured and corrected angular distribution for the 344 keV - 778 keV cascade in ^{152}Gd

Figure 4.15: Angular correlation correction for the tracked γ-ray efficiency for the 344 keV - 778 keV cascade in ^{152}Gd

Chapter 5

Analysis of the experiment

The commissioning experiment of the AGATA + PRISMA setup involved a ^{32}S beam at 160 MeV impinging on a ^{124}Sn target. The main aim of the experiment was to observe well known nuclei in order to test the performances of the coupling of the two detection systems. Additionally, a study of the structure of the populated nuclei in the multi-nucleon transfer reaction will be performed, thanks to the PRISMA A and Z identification coupled with the γ-ray detection capabilities of AGATA and using a time coincidence window between the two systems.

The setup included two different targets: one thin target of 0.5 mg/cm^2 and a thick one of 2.5 mg/cm^2. The processing of PRISMA and the following analysis of the γ rays in this work was performed only for the runs with the thin target.

5.1 γ-ray spectroscopy with multi-nucleon transfer reactions

The reaction mechanism that is the focus of this experiment is multi-nucleon transfer. In this type of reactions one or more nucleons are transferred between the two heavy ions that are the beam and the target. The advantage of using this type of reactions is the possibility to produce neutron-rich nuclei that would not be accessible with other reaction mechanisms. As these reactions are binary processes, two nuclei are produced at the same time. One is a beam-like fragment that exits the target and is detected by PRISMA in this setup. The other is a target-like nucleus which is also called *binary partner*. In a reaction, therefore, both of these nuclei may be produced in an excited state and γ rays might be emitted by both of them. By selecting a transfer channel thanks to PRISMA, the involved isotopes are fixed, but the γ rays detected in coincidence in AGATA come, in principle, from both of the produced nuclei. The way to differentiate between the spectrum that belongs to the beam- or target-like nucleus is thanks to the Doppler correction.

5.1.1 Doppler correction

Every γ ray that is emitted in flight by nuclei at relativistic velocities undergoes a Doppler shift depending on the angle of emission with respect to the flight direction of the particle and the modulus of its velocity. Thanks to AGATA PSA and tracking algorithms, the first-interaction point in the array of each detected γ ray is obtained with good precision and the Doppler correction can be performed event-by-event by knowing the velocity vector $\vec{\beta}$ of the emitting nucleus.

While for the beam-like fragment, the $\vec{\beta}$ is given by PRISMA, the velocity vector of the binary partner is obtained through a kinematic reconstruction of the binary reaction. This is possible because the conditions before the reaction are well known, being the beam energy selected beforehand, and because PRISMA gives information about both the energy and the direction of the beam-like fragment. Therefore, knowing the ground-state-to-ground-state Q value of the transfer it is possible to obtain the $\vec{\beta}_{BP}$ for the Doppler correction of the γ rays of the binary partner.

5.1.2 Channel population

After PRISMA processing and calibrations, the distribution of the A and Z of the beam-like fragments can be obtained from the experimental data. The quasi-elastic channel with ^{32}S as ejectile is the most populated channel, where among the identified events from PRISMA, around 62.9% belong to this channel. Other strong channels are the neutrons transfer that produce another S isotope, especially $+1n$ (^{33}S) and $+2n$ (^{34}S), or the protons transfer channels as the $-1p$ (^{31}P), $-2p$ (^{30}Si).

In this work, the focus of the analysis of the γ rays was on one specific channel: the $-2p$ channel, that involves the reaction ^{124}Sn(^{32}S,^{30}Si)^{126}Te. Among the identified events, the ratio of the number of events in the $-2p$ channel with respect to the quasi-elastic channel is 9.9%.

5.2 Analysis of the (^{32}S,^{30}Si) transfer channel

The $-2p$ transfer channel (^{32}S,^{30}Si) is examined in this work in order to evaluate the goodness of the Doppler corrected spectra and to reconstruct level schemes of the populated nuclei. In this case, the final nuclei are ^{30}Si as the beam-like and ^{126}Te as the target-like (binary partner).

Examining the γ-ray energy spectra in coincidence with this transfer channel, it is possible to compare the Doppler correction performed on either the beam-like product or the target-like one. Figure 5.1 compares the non-corrected spectrum, the spectrum corrected for ^{30}Si and the spectrum corrected for ^{126}Te. The energies of the most intense γ rays for ^{30}Si are indicated with blue dashed lines, and the ones for ^{126}Te are given by red dashed lines. In the non-corrected spectrum and in the one with the correction for the binary partner, the peaks of ^{30}Si are not visible. The events which make up the photo-peaks in the spectrum with the right Doppler correction, produce a broad distribution in the spectra with the wrong correction. An example

of this is given by the peak at ∼2235 keV of ^{30}Si in fig. 5.1, where it is highlighted in yellow in all three spectra, but only in the spectrum corrected for ^{30}Si, the shape resembles a peak.

Therefore, the analysis of the γ rays emitted by ^{30}Si was performed in the spectrum with the Doppler correction on the beam-like $\vec{\beta}$, while the γ rays of ^{126}Te were observed in the spectrum corrected for the $\vec{\beta}$ of the binary partner. The average measured β for the ^{30}Si ejectiles is $\sim 8.8\%$ and the average reconstructed β for the ^{126}Te recoil is $\sim 2.2\%$. For the analysis of the spectra, the Cubix software, as part of the Gammaware package, was used [45].

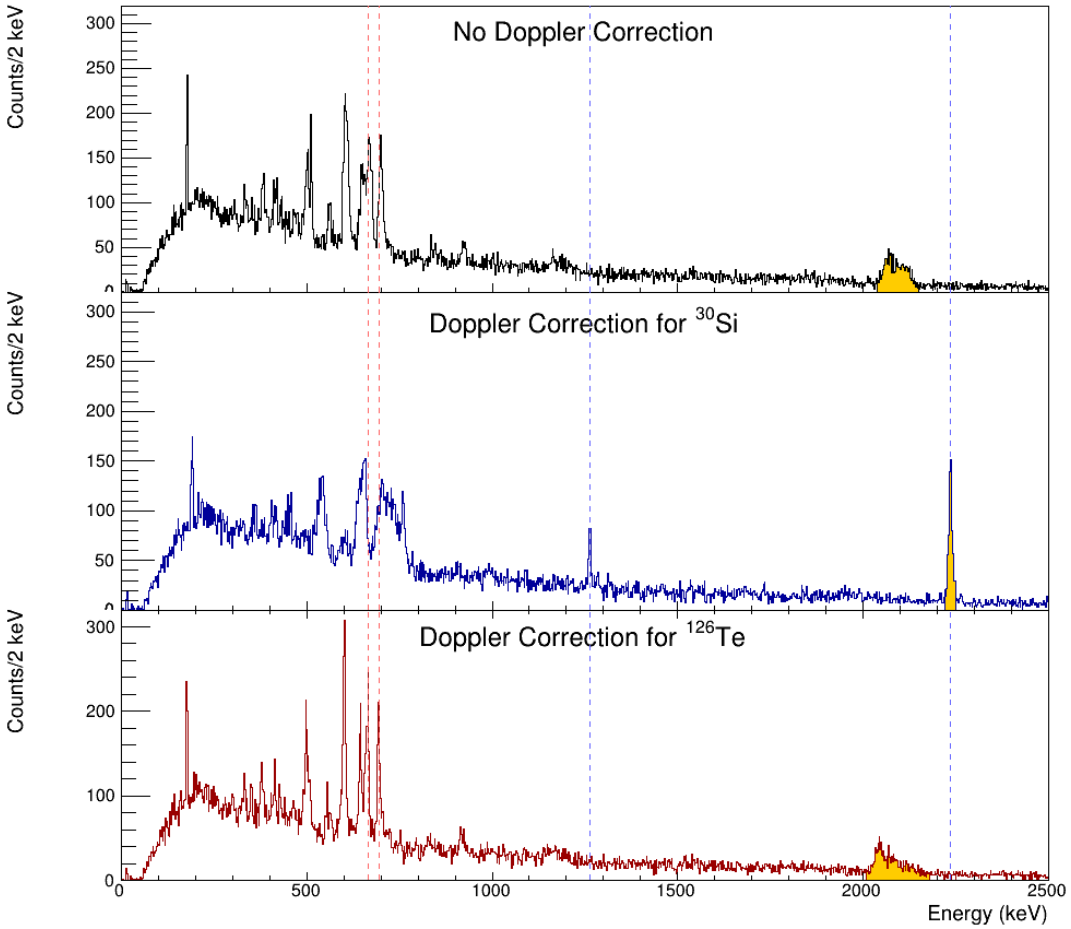

Figure 5.1: Spectrum of the γ rays in coincidence with ^{30}Si with different Doppler corrections: No Doppler correction (top), Doppler correction for ^{30}Si (middle) and Doppler correction for the binary partner ^{126}Te (bottom).

5.2.1 Beam-like fragment

As for the γ-ray energy spectrum with the Doppler correction on ^{30}Si, all the observed peaks were above 1 MeV. The detail of the spectrum with the recognized transitions is shown in fig. 5.2. Comparing the energy of the centroids with the available data on ^{30}Si, the peaks were assigned to known transitions between the levels of the nucleus [46]. The details of the fits of the peaks are reported in table 5.1. In the table the energy of the γ ray E_γ, the energy of the centroid E_{exp}, the FWHM of the peak, the energy resolution R as defined in eq. 4.2, the raw counts

and the relative intensity I_{rel} of the γ ray are reported. The relative intensity is calculated by correcting the counts for the detection efficiency at the centroid energy with the curve obtained thanks to source measurements (tracked γ rays) reported in table 4.3, and then normalizing them to the area of the $2^+ \rightarrow 0^+$ peak at 2236.0 keV.

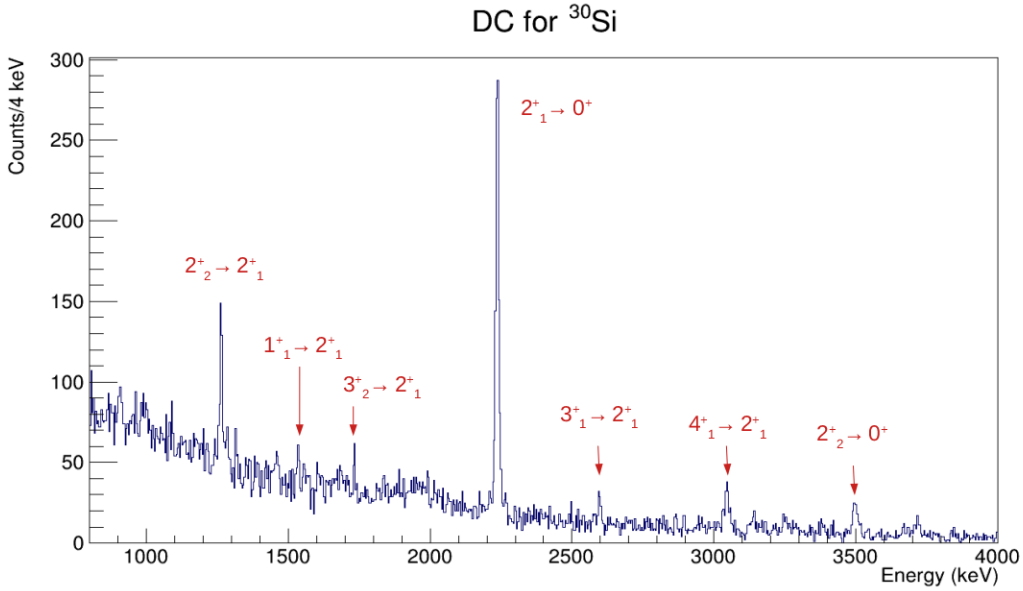

Figure 5.2: Doppler-corrected spectrum for the beam-like fragment with identified transitions in the level scheme of ^{30}Si.

Table 5.1: γ rays in the Doppler corrected spectrum for ^{30}Si. Intensities are calculated from efficiency-corrected areas and normalized to the 2236.0 keV transition.

E_γ (keV)	E_{exp} (keV)	FWHM (keV)	R (‰)	Area	I_{rel}
1263.13(3)	1264.0(4)	4.7(16)	3.7(13)	252 (32)	0.19 (3)
1534.12(4)	1535.4(9)	6.8 (18)	4.4(12)	60 (15)	0.051 (13)
1732.7(1)	1732.0(4)	6.6 (13)	3.8(8)	46 (14)	0.041 (13)
2235.23(2)	2236.0(2)	7.8(9)	3.5(4)	983 (63)	1.00 (10)
2595.39(4)	2596.8(10)	10.4 (17)	4.0(7)	58 (15)	0.064 (17)
3043.2(1)	3047.3(12)	11(3)	3.6(10)	134 (23)	0.16 (3)
3498.33(5)	3496.0(13)	13(4)	3.6(11)	123 (22)	0.16 (3)

The centroids of the fitted peaks agree with the reported energies within < 1.5 keV in all cases, beside the two transitions at energy higher than 3 MeV. For the 3496.0 keV transition, the discrepancy is more than 2 keV, while for the 3047.3 keV transition, the centroid is over 4 keV distant from the reported energy.

This means that the Doppler correction reconstructs the peaks around the correct energy, with most γ rays except the two highest ones in energy. Further analysis will be performed to understand these two discrepancies, although they might be related to some parameters in the Doppler correction calculation that need a better calibration. A fine tuning of the Doppler correction may be performed by checking the correctness of the β due to the ToF calibration in

PRISMA, or the geometry might be adjusted through shifts or rotations in the position of the PRISMA MCP or the AGATA detectors for the θ calculation.

The energy resolution of the peaks is around $3.5-4‰$, which is a higher value than the resolution measured with the sources, which after 1 MeV settles around $2-2.5‰$ as seen from fig. 4.9. Getting a worse resolution is expected, because after the Doppler correction, the calculation of the energy takes into account also the resolution in the estimation of β and θ. This result is still much better than the typical resolution after the Doppler correction with a standard HPGe detector, such as CLARA, which would be around $6-9‰$ [47].

By doing a linear extrapolation of the trend of the FWHM as function of the energy at $E_\gamma > 700$ keV from the graph in fig. 4.8, one expects a FWHM of ~ 3.6 keV for the peak at 2236.0 keV for the γ ray emitted at rest, while 7.8(9) keV is the measured value after the Doppler correction. If this extrapolation is rescaled by the ratio of the Doppler-corrected value to the expected value at rest for the peak at 2236.0 keV, the predicted FWHM at 3047.3 keV is ~ 9.1 keV. The measured value of 11(3) keV is higher, but it is compatible within the uncertainty. Similar results are obtained for the other peaks. This means that the measured FWHM values of the Doppler-corrected peaks increase with energy in a similar way to the trend observed with the source measurements, after taking into account the worsening of resolution given by the Doppler correction.

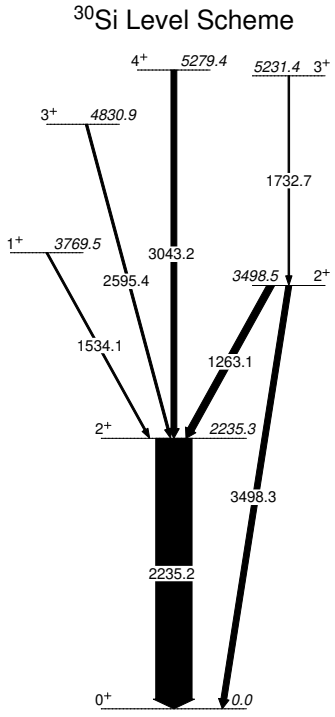

Figure 5.3: Partial level scheme of the excited states of ^{30}Si populated in the $2p$ transfer from ^{32}S. The energies of the levels and the transitions are in keV.

A level scheme with the identified transitions was built and displayed in fig. 5.3. The widths of the arrows represent the relative intensity of the transitions.

5.2.2 Target-like fragment

An analysis of the spectrum with the Doppler correction for the binary partner was performed in a similar way to the one for the beam-like fragment. The analysis yielded several peaks that are located in a lower energy range, around $[150, 800]$ keV (fig. 5.4). By comparing all these peaks with the known γ rays of ^{126}Te, only three transitions match [48]. The rest of the peaks were found to belong to other isotopes of Te, in particular those ranging from $A = 123$ to $A = 125$ [49–51].

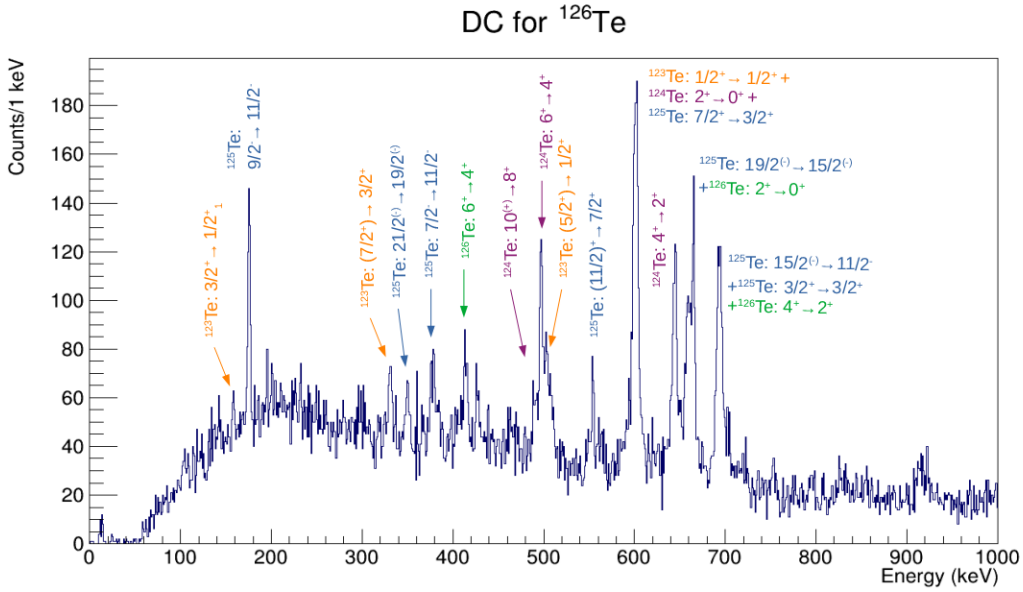

Figure 5.4: Doppler-corrected spectrum for the target-like fragment with identified transitions in the level scheme of different Te isotopes: ^{126}Te (green), ^{125}Te (blue), ^{124}Te (purple) and ^{123}Te (orange).

The observation of the γ rays of neighbouring Te isotopes is not given by a contamination in the gating, but it is due to the evaporation of neutrons after the transfer reaction. When ^{126}Te is populated with high enough energy, it can evaporate a number of neutrons and therefore produce the neighbouring isotopes of Te with $N-1, N-2, ...$ In this way the γ rays of those nuclei are emitted during their de-excitation and they appear in coincidence with the ^{30}Si fragment. This effect is well known, for example one can see a similar case in a multi-nucleon transfer experiment with the PRISMA + CLARA setup in ref. [47]. Effectively, only $\sim 10\%$ of the γ rays come from ^{126}Te, therefore there is a high chance to evaporate at least one neutron.

The way to select only the γ rays coming from the de-excitation of ^{126}Te is to put a condition on the excitation energy of the final system. In fact, PRISMA also gives the total kinetic energy loss of the reaction (also called *reconstructed Q value*) [26] by comparing the initial conditions with the detected energy and direction of the beam-like ejectile and taking into account the ground-state-to-ground-state Q value of the transfer reaction. This energy difference can be

regarded as the $-Q$ value of the reaction and equals the sum of the excitation energies of beam-like and target-like fragments. By selecting a maximum value for the $-Q$ value and looking at the corresponding γ spectrum it is possible to exclude most of the events where neutron evaporation happened.

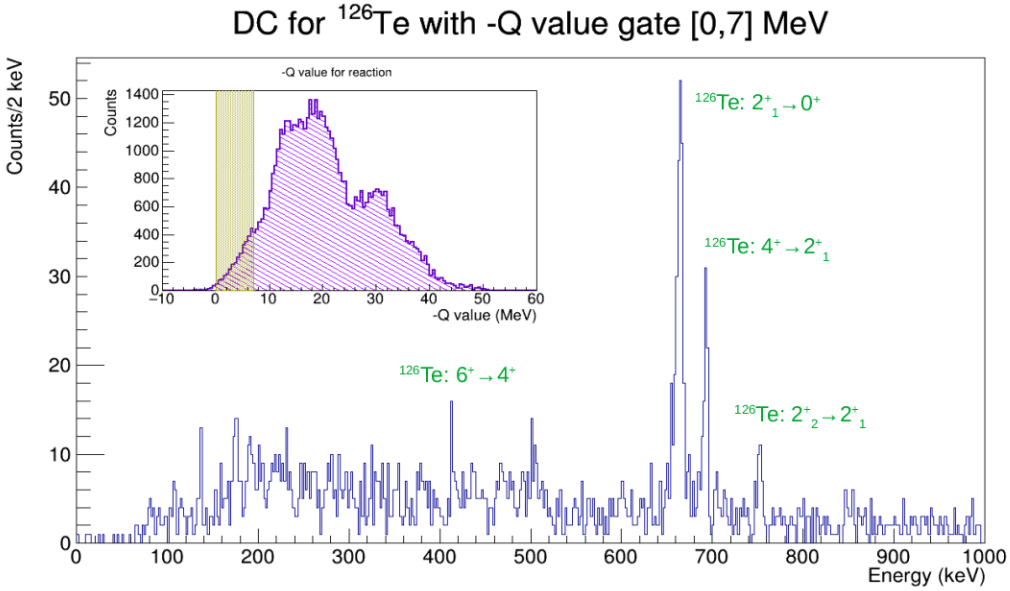

Figure 5.5: Doppler-corrected spectrum for the target-like fragment with a gate of [0,7] MeV on the $-Q$ value. The identified peaks of ^{126}Te are labeled in green. The inset shows the distribution of the reconstructed $-Q$ value with the area of the gate highlighted in yellow.

Table 5.2: γ rays in the Doppler corrected spectrum for ^{126}Te. Intensities are calculated from efficiency-corrected areas and normalized to the 664.9 keV transition.

E_γ (keV)	E_{exp} (keV)	FWHM (keV)	R (‰)	Area	I_{rel}
414.82(6)	413.0(10)	4(2)	9(6)	26(10)	0.10(4)
666.337(12)	664.9(5)	6.8(7)	10.3(11)	225(30)	1.00(19)
695.03(2)	694.0(6)	3.9(14)	6(2)	83(18)	0.38(10)
753.822(13)	752.5(6)	5.0(11)	6.6(15)	24(10)	0.11(5)

Figure 5.5 shows the γ-ray spectrum with the Doppler correction for ^{126}Te and with the condition on the excitation energy ($-Q$) to be in the range $[0, 7]$ MeV. In this spectrum, the identified peaks belong exclusively to ^{126}Te and the contamination from the evaporation residues is suppressed. Table 5.2 shows the energy of the γ ray E_γ, the energy of the centroid E_{exp}, the FWHM of the peak, the energy resolution R as defined in eq. 4.2, the raw counts and the relative intensity I_{rel} of the γ rays.

The transitions were associated with the known ones in ^{126}Te [48]. In this case, the discrepancy between the centroids of the peaks and the known energies is around 1-1.5 keV for all the peaks, with the measured energies systematically at lower values. Although this is not outside a 3σ interval with respect to the fits, it can be a symptom of an inaccurate Doppler correction. Just as in the beam-like case, further optimization of the parameters in the calculation of the angles and

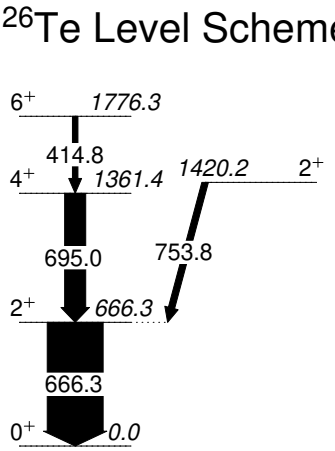

Figure 5.6: Partial level scheme of the excited states of ^{126}Te observed with a gate of $[0, 7]$ MeV in the excitation energy of the reaction. The energies of the levels and the transitions are in keV.

velocities for the Doppler correction is needed to check the correctness of this reconstruction. In the Doppler correction of the binary partner, the $\vec{\beta}$ is not directly measured, but it is deducted by the reconstruction of the binary reaction with the $\vec{\beta}$ of the beam-like fragment, taking into account also the energy losses of the fragments in the target and assuming that the reaction occurs at its center. This means that the worsening of the resolution with this correction will be even more significant, due to the added uncertainty on the reaction exact position. The energy resolution of the peaks is around $6 - 9$‰, with the most intense peak at 664.9(5) keV reaching a value of 10.3(11)‰. As expected, the resolution is worse compared to the beam-like spectrum, also because the transitions are at a lower energy. The large width of the $2^+ \rightarrow 0^+$ is in disagreement with the rest of the measured widths, so further analysis will be required to understand this behaviour. As explained for the previous spectrum, the Doppler correction might require adjustments in order to obtain better peak widths and an analysis of fine tuning of the ToF, the MCP position and AGATA geometry will be performed in the future.

Comparing the observed peaks with the known transitions in ^{126}Te [48], the level scheme was built, fig. 5.6. The widths of the arrows represent the relative intensity of the transitions.

5.3 Discussion of the results

The analysis of the γ spectra shows that, in the case of the beam-like fragment (^{30}Si) the identified γ rays in the Doppler-corrected spectrum correspond to the selected nucleus in the PRISMA (A, Z) gate. This means that the PRISMA-AGATA coincidence is working correctly. The Doppler-corrected peak centroids are in agreement with the known energies, except for the two peaks over 3 MeV, which are 2.5-4 keV off the reported energy. This shows that the Doppler correction needs further improvement by optimizing the parameters in the MCP and AGATA geometry and in the calibration of the Time of Flight.

In the binary partner Doppler-corrected spectrum, γ rays from several Te isotopes are observed, as a result of neutron evaporation after the transfer reaction. By placing a gate in the low excitation energy ($-Q$) region, it is possible to restrict the analysis to the γ rays of ^{126}Te. The Doppler correction shows a small systematic shift in the centroids of the peaks for the spectrum of the binary partner, that shows that some optimization can be performed in the analysis and Doppler correction. Since the calculation of the $\vec{\beta}$ of the target-like fragment involves assumptions on the position of the binary reaction, an optimization of the calculation of the $\vec{\beta}$ of the beam-like is needed to obtain a good correction for the target-like as well. Furthermore, the calculation of the energy losses in the target may be checked as it affects the modulus of the β of the binary partner.

The average energy resolution for the beam-like fragment spectrum is 3.8‰, while for the target-like the resolutions range between $6 - 10$‰. Comparing these estimates with the resolution measured with the sources, a worsening in energy resolution is observed. In the first place, this is caused by the inclusion of the resolution in β and θ in the Doppler correction. However, especially in the case of the target-like fragment, a fine tuning of the parameters involved in the Doppler correction might be needed.

For the two populated nuclei: ^{30}Si and ^{126}Te, level schemes were built and the relative intensities of the observed transitions were calculated, by taking into account also the efficiency of tracked γ rays in AGATA. Six excited levels were observed in the analysis of ^{30}Si, among which the yrast 4^+ and 2^+. In the analysis of ^{126}Te, four excited states were observed and the yrast 6^+, 4^+, 2^+ and the second 2^+ were populated.

These result show the capabilities of the coupling AGATA + PRISMA in the study of structure of nuclei populated by multi-nucleon transfer reactions. A few steps in the analysis may still need fine tuning to obtain better energy resolution in the γ spectra, especially with the Doppler correction, but one could say that the commissioning experiment to test the coupling of AGATA to PRISMA was successful.

Chapter 6

Conclusions

6.1 Summary

The Advanced GAmma Tracking Array (AGATA) is a γ-ray tracking detector which represents the state-of-the-art for high-resolution γ-ray spectroscopy. Its digital acquisition electronics allows to perform Pulse Shape Analysis (PSA) of the signals and localize the interaction points of the photons in the HPGe crystals. A γ-ray tracking algorithm is then applied to reconstruct the trajectories of the γ rays within the array and recover a higher number of photo-peak events. After the recent installation of AGATA at the National Laboratories of Legnaro (LNL) in Italy, a series of commissioning experiments were performed to test AGATA with the available complementary detectors.

The work in this thesis focused on the optimization of the data processing of AGATA and the evaluation of the performances of the setup with radioactive sources and in the first in-beam commissioning experiment, where the AGATA array was coupled to the PRISMA magnetic spectrometer.

The first part of the work dealt with the optimization of the pre-sorting of the AGATA data. For every step of the processing from the digitized traces to the γ-ray spectra after the tracking algorithm, the calibration and correction parameters were calculated using radioactive sources. The effects which were corrected in the sorting process included the cross-talk between channels in the segmented crystals and the partial collection of charge in the germanium due to neutron bombardment damage in the semiconductor lattice. After the time and energy calibration of all the channels, the Pulse Shape Analysis algorithm was used to locate the hits in the germanium with a precision of around 5 mm. From the detected interactions, the tracking reconstruction was performed to increase the efficiency and the peak-to-total ratio of the spectra.

After the optimization of the various steps in the processing, measurements with radioactive sources were used to evaluate the performance of the array in terms of energy resolution, efficiency and peak-to-total. Simulations of the same sources were also performed and compared with the measured values. For the 1.3 MeV peak of ^{60}Co, the measured FWHM was approxi-

mately 2.77 keV for the core spectrum and 2.92 keV for the tracked one. Considering 23 HPGe crystals at the nominal position, the absolute efficiency at 1.3 MeV was estimated to be 2.52(7)% and 3.24(9)%, respectively for the core and the tracked spectra, and the estimated peak-to-total ratios were, respectively, around 17.4% and 30.3%.

The commissioning experiment consisted in a multi-nucleon transfer reaction with a ^{32}S beam at 160 MeV on a ^{124}Sn target. The sorted and calibrated data from PRISMA were merged to the γ-ray data from AGATA with a time coincidence. Through the (A, Z) identification of the ejectile nuclei in PRISMA, it was possible to study the γ-ray spectra in coincidence with specific transfer channels. In this work, the analysis focused on the $-2p$, *i.e.* the ^{30}Si and ^{126}Te binary partners produced in the transfer process.

The Doppler correction of the γ rays emitted in flight was performed event-by-event with the $\vec{\beta}$ of the beam-like ejectile measured by PRISMA and the first interaction hit of every reconstructed photon from the PSA and the tracking algorithm. To obtain the Doppler-corrected spectrum emitted by the target-like fragment, the $\vec{\beta}$ was calculated via a reconstruction of the binary reaction.

From the analysis of the spectra, several transitions belonging to ^{30}Si were identified and a level scheme was built. In the spectrum with the Doppler correction for ^{126}Te, several peaks belonging to other Te isotopes were identified, produced after neutron evaporation following the transfer process. By placing a gate on the $-Q$ value of the reaction, an energy spectrum was obtained where only the γ rays of ^{126}Te were observed, and a level scheme was built with the identified transitions.

6.2 Future perspectives

The results of the commissioning experiment obtained in the work of this thesis have proved the capabilities of the AGATA + PRISMA coupling for the selection of reaction channels and the Doppler correction of the γ rays that are emitted in flight. The measured energy resolution of the peaks after the Doppler correction shows the higher performances in using the AGATA tracking array with respect to a standard HPGe detector. The analysis in this thesis showed that for a few transitions, the Doppler correction shows inaccuracies in the reconstructed peak centroid energy. A work of finer optimization will follow these results in order to set the optimal parameters that are involved in the calculation of the Doppler correction, such as the calibration of the PRISMA Time of Flight, or a better setting of the geometry of the MCP or of the AGATA detectors.

The installation of AGATA at LNL and the coupling with different complementary detectors will allow to perform different types of experiments with stable nuclei. Especially, the high selectivity of the AGATA-PRISMA coincidence is a very powerful tool that can be used to observe γ rays in systems that are far more exotic than in the studied experiment. An example of the use of this setup for nuclear structure studies is the experiment of fusion-fission to perform γ-ray

spectroscopy of the region of $N = 50$ close to the double magic ^{78}Ni, which was already approved by the LNL PAC [52]. In the proposed configuration, the nuclei of interest will be produced as fission fragments after the fusion of ^{208}Pb+^{9}Be, and the selectivity of the PRISMA+AGATA setup will be essential to select the reaction channel in order to observe the γ rays of the populated levels. Since this experiment involves γ-ray spectroscopy in a very neutron-rich region, the expected yields of the relevant transitions are limited and therefore the efficiency and sensitivity of AGATA are essential for this study.

Bibliography

[1] G. F. Knoll. *Radiation Detection and Measurement*. Wiley, 2000.

[2] J.F. Sharpey-Schafer and J. Simpson. *Progr. Part. Nucl. Phys.*, 21:293–400, 1988.

[3] J. Simpson. *Zeit. Phys. A*, 358:139–143, 1997.

[4] I. Lee. *Nucl. Phys. A*, 520:641–655, 1990.

[5] S. Akkoyun et al. *Nucl. Instr. Meth. A*, 668:26–58, 2012.

[6] I. Y. Lee et al. *Nucl. Phys. A*, 746:255–259, 2004.

[7] A. Gadea et al. *Nucl. Instr. Meth. A*, 654:88–96, 2011.

[8] N. Lalovic et al. *Nucl. Instr. Meth. A*, 806:258–266, 2016.

[9] E. Clément et al. *Nucl. Instr. Meth. A*, 855:1–12, 2017.

[10] Valiente-Dobón et al. *Nucl. Instr. Meth. A*, in preparation.

[11] A. M. Stefanini et al. *Nucl. Phys. A*, 701(1):217–221, 2002.

[12] M. Rocchini et al. *Nucl. Instr. Meth. A*, 971:164030, 2020.

[13] C. Müller-Gatermann et al. *Nucl. Instr. Meth. A*, 920:95–99, 2019.

[14] F. Crespi et al. Commissioning of agata and complementary detectors at LNL. Proposal.

[15] `https://www.lnl.infn.it`.

[16] C. Signorini et al. *Nucl. Instr. Meth. A*, 244(1-2):27–30, 1986.

[17] C. A. Ur. *AIP Conference Proceedings*, 1530:35, 2013.

[18] A. Pullia et al. *IEEE Symposium Conference Record Nuclear Science*, 3:1411–1414, 2004.

[19] G. Benzoni et al. *INFN-LNL Annual Report*, 266:41–42, 2022.

[20] B. Bruyneel et al. *Eur. Phys. J. A*, 52:70, 2016.

[21] R. M. Pérez Vidal. PhD thesis, Universidad de Valencia, 2019.

[22] F. Recchia et al. *Nucl. Instr. Meth. A*, 604:555–562, 2009.

[23] R. Venturelli and D. Bazzacco. *LNL Annual Report 2004*, page 220, 2005.

[24] L. Lewandowski et al. *Eur. Phys. J. A*, 55(5), 2019.

[25] A. Lopez-Martens et al. *Nucl. Instr. Meth. A*, 533:454–466, 2004.

[26] F. Galtarossa. PhD thesis, Università degli studi di Ferrara, 2016.

[27] G. Montagnoli et al. *Nucl. Instr. Meth. A*, 547:455–463, 2005.

[28] S. Beghini et al. *Nucl. Instr. Meth. A*, 551:364–374, 2005.

[29] X. Grave et al. *14th IEEE-NPSS Real Time Conference 2005*, page 5, 2005.

[30] B. Bruyneel et al. *Nucl. Instr. Meth. A*, 599:196–208, 2009.

[31] B. Bruyneel et al. *Nucl. Instr. Meth. A*, 608:99–106, 2009.

[32] https://atrium.in2p3.fr/nuxeo/nxdoc/default/878272cd-bb33-4b35-aa30-227c1a38e8d1/view_documents.

[33] B. Bruyneel et al. *Eur. Phys. J. A*, 49:61, 2013.

[34] F. Mijatović. PhD thesis, University of Zagreb, 2016.

[35] E. Pilotto. Master's thesis, Università degli studi di Padova, 2022.

[36] D. Montanari. PhD thesis, Università degli studi di Milano, 2009.

[37] E. Farnea. *Nucl. Instr. Meth. A*, 621:331–343, 2010.

[38] S. Agostinelli. *Nucl. Instr. Meth. A*, 506(3):250–303, 2003.

[39] I. Zanon. PhD thesis, Università degli studi di Ferrara, 2021.

[40] M. Lebiche. Agata simulation workshop, 2022.

[41] D. C. Radford. *Nucl. Instr. Meth. A*, 361(1-2):297–305, 1995.

[42] http://bricc.anu.edu.au/index.php.

[43] H. Morinaga and T. Yamazaki. *In-beam gamma-ray spectroscopy*. North- Holland, 1976.

[44] https://radware.phy.ornl.gov/gf3/gf3.html.

[45] https://atrium.in2p3.fr/nuxeo/nxpath/default/Atrium/sections/Public/AGATA/DataProcessing/GRSCookbook@view_documents?

[46] M. Shamsuzzoha Basunia. *Nucl. Data Sheets*, 111:2331, 2010.

[47] S. Szilner et al. *Phys. Rev. C*, 76:024604, 2007.

[48] H. Iimura et al. *Nucl. Data Sheets*, 180:1, 2022.

[49] J. Katakura. *Nucl. Data Sheets*, 112:495, 2011.

[50] J. Katakura and Z. D. Wu. *Nucl. Data Sheets*, 109:1655, 2008.

[51] J. Chen. *Nucl. Data Sheets*, 174:1, 2021.

[52] A. Gottardo et al. Fusion-fission for γ-ray spectroscopy of neutron-rich nuclei around n = 50. Proposal.